The brittle-to-viscous transition in polycrystalline quartz: An experimental study

Bettina Richter, Holger Stünitz, Renée Heilbronner

Accepted Manuscript

The brittle-to-viscous transition in polycrystalline quartz: An experimental study

Bettina Richter, Holger Stünitz, Renée Heilbronner

PII: S0191-8141(18)30275-X

DOI: 10.1016/j.jsg.2018.06.005

Reference: SG 3676

To appear in: *Journal of Structural Geology*

Received Date: 29 September 2017

Revised Date: 3 June 2018

Accepted Date: 3 June 2018

Please cite this article as: Richter, B., Stünitz, H., Heilbronner, René., The brittle-to-viscous transition in polycrystalline quartz: An experimental study, *Journal of Structural Geology* (2018), doi: 10.1016/j.jsg.2018.06.005.

The brittle-to-viscous transition in polycrystalline quartz: an experimental study.

Bettina Richter[1], Holger Stünitz[2,3], Renée Heilbronner[1,2]

[1]*Geological Institute, Basel University, Bernoullistrasse 32, 4055 Basel, Switzerland*

[2]*Department of Geology, Tromsø University, Dramsveien 201, 9037 Tromsø, Norway*

[3]*Institut des Sciences de la Terre d'Orléans (ISTO), Université d'Orléans, 45071 Orléans, France*

Corresponding author: Renée Heilbronner (renee.heilbronner@unibas.ch)

Keywords (4-6):

brittle-to-viscous transition, grain size distribution, dislocation creep, quartz rheology, stress exponent

Abstract (<250 words)

Shear experiments on quartz gouge were performed at elevated confining pressures (predominantly 1.5 GPa) and temperatures (500 °C - 1000 °C) at shear strain rates of $3.5 \cdot 10^{-6}$ s^{-1} to $2 \cdot 10^{-3}$ s^{-1} to study the brittle-to-viscous transition. An unsystematic temperature dependence of strength at low temperatures changes towards a clear temperature weakening dependence above 650 °C. The transition from a pressure strengthening to a pressure weakening relationship takes place continuously between 650 °C and 800 °C. Strain rate stepping experiments reveal power-law breakdown at low temperatures (~650 °C). Between 800 °C and 1000 °C, a stress exponent of n = 1.9 ± 0.6 and an activation energy of Q = 170 ± 72 kJ/mol indicate a combination of diffusion and dislocation creep. The Goetze criterion is confirmed as the upper stress limit for viscous deformation mechanisms. Localised deformation in the form of

semibrittle shear bands with Riedel geometry at low temperatures changes to homogeneous deformation with a pervasive foliation accompanied by a continuous texture evolution between 700 °C and 1000 °C. Fracturing dominates at low temperatures accompanied by increasing amounts of dissolution and precipitation in fine-grained zones with increasing temperature. Above 650 °C, dislocation and diffusion creep are the dominating deformation processes, with dislocation creep being favoured in larger grains while dissolution-precipitation is active in the fine-grained fraction.

1. Introduction

The transition from fully brittle to fully viscous deformation in rocks (semi-brittle field) occurs over a broad range of conditions in pressure, temperature, strain rate, and H_2O-content with several changes in deformation mechanisms (e.g., *Kohlstedt et al.*, 1995; *Scholz*, 2007; *Hirth and Tullis*, 1994). Viscous denotes temperature- and strain-rate dependent deformation here. In the lithosphere, the transition commonly takes place within the middle crust (continents) (e.g., *Brace and Kohlstedt, 1980*; *Handy*, 1989; *Sibson*, 1989) but it may extend into the upper mantle for some rocks, e.g., below the oceanic crust (e.g., *Kohlstedt et al.*, 1995). The transition region coincides with the greatest strength of rocks, and many large earthquakes nucleate in this region (e.g., *Sibson*, 1989; *Scholz*, 2007).

Under conditions of brittle deformation (e.g., low temperatures, high strain rates, typically shallow crustal levels), the strength of rocks primarily depends on normal stress and pore pressure (*Byerlee*, 1978). Fracture strength and/or friction control the rock deformation, leading to cataclastic processes (e.g., fracturing, frictional sliding) with characteristic microstructures at greater strain. The intersection

of Byerlee's law (*Byerlee*, 1978) with the Mohr-Coulomb fracture criterion marks the onset of semi-brittle deformation in most lithologies (e.g., *Kohlstedt et al.*, 1995). This intersection is termed “brittle-ductile transition” and is temperature independent. Viscous deformation at higher temperature, typically at deeper crustal levels, depends on strain rates and temperatures, and is caused by diffusion and/or dislocation creep involving recovery processes like dynamic recrystallisation (e.g., *Poirier and Guillope*, 1979; *Tullis and Yund*, 1977; *Yund and Tullis*, 1991; *Hirth and Tullis*, 1994; *Tullis*, 2002). The transition from semibrittle to viscous deformation is marked by the brittle-to-viscous-transition (*Kohlstedt et al.*, 1995) (BVT). The Goetze criterion has been introduced as an ad hoc approximation by Kohlstedt et al. (1995) to delineate this transition. It is formulated as $\Delta\sigma = Pc$, i.e. the differential stress to drive viscous flow is equal to the confining pressure.

In the transitional semi-brittle zone, stresses required to create new fractures are lower than those for sliding on pre-existing faults (e.g., *Byerlee*, 1968; *Kohlstedt et al.*, 1995) causing pervasive fracturing and grain-size reduction (cataclasis). Dislocations may be generated by cracking and healing processes (e.g., *FitzGerald et al.*, 1991; *Tarantola et al.*, 2012; *Trepmann and Stöckhert*, 2013; *Stünitz et al.*, 2017), but whether these dislocations become important for crystal plasticity (dislocation creep) depends on temperature and the efficiency of the recovery processes. At low temperatures, tangling dislocations and high dislocation densities produce strain hardening and greater stresses (e.g., *Barber et al.*, 2010). Dominant crystal plasticity is achieved at higher temperatures, where dislocation climb and recrystallisation are rate controlling. For quartz, three types of dislocation creep regimes have been identified dependent on the dominance of subgrain-rotation recrystallization or grain-boundary migration (*Hirth and Tullis*, 1992).

Grain size reduction by cracking may play an important role for the onset of viscous deformation by increasing the surface area and decreasing the transport distances, leading to accelerated mass-transfer processes (e.g., *Pec et al.*, 2012; *Trepmann and Stöckhert*, 2003; *Menegon et al.*, 2008; *Van Daalen et al.*, 1999). As a result, deformation by diffusion creep may become the dominant mechanism should such cracking occur (e.g., *Paterson*, 2013, p. 91-105, and references therein).

It emerges from this brief discussion that in the transition region of brittle-to-viscous deformation, several processes are competing: cracking and frictional sliding, crystal-plastic deformation, and diffusive mass transfer combined with friction-less grain-boundary sliding. This study will try to address their relative importance for deformation in quartz over a range of temperatures and confining pressures.

Quartz as one of the most abundant silicates in the Earth´s crust is often used to model and predict the mechanical behaviour of the upper lithosphere (e.g., *Brace and Kohlstedt*, 1980). In addition, deformation mechanisms in quartz can be studied independently of chemical effects because of its simple chemistry and very limited compositional variation. Laboratory conditions (e.g., high strain rates: 10^{-3}-10^{-7} s^{-1}, high temperatures) have been extrapolated to natural conditions (e.g., low strain rates: 10^{-10}-10^{-14} s^{-1}, low temperatures) via flow laws that are applicable for viscous deformation (e.g., *Jaoul et al.*, 1984; *Kronenberg and Tullis*, 1984; *Paterson and Luan*, 1990; *Luan and Paterson*, 1992; *Gleason and Tullis*, 1995; *Hirth et al.*, 2001; *Rutter and Brody*, 2004a,b). However, few data exist to define the lower temperature limit of the applicability of these flow laws. Futhermore, discrepancies exist for the parameters of flow laws, so that the uncertainty for the users as to which data to use is large, calling for a better characterisation of rheological properties of quartz.

We present a series of deformation experiments on quartz in a modified Griggs

apparatus to study the rheological transition from brittle-to-viscous deformation mechanisms at elevated pressures and temperatures. The goal is to determine the part of the pressure-temperature-strain rate-range of the transition accessible in the laboratory and to extrapolate it to natural conditions. Some rheological parameters determined for quartz fault-rock material in this study can be used in flow laws for quartz. The extrapolation of the conditions of the brittle-to-viscous transition to natural fault zones will be discussed, together with some applications of the newly determined parameters for the flow law.

2. Methods

2.1 Experimental method

The experiments were carried out on a crushed quartz crystal from a hydrothermally grown single crystal from an Alpine cleft (Aar Massif, Switzerland). Pieces of the crystal were repeatedly crushed and sieved to obtain a grain-size fraction below 100 µm, used for what will be considered the standard experiments (referred to as 'crushed'). One sample had a grain size range of 7-11 µm (referred to as 'sieved'). The single crystal contained several fluid inclusions (5-200 µm) (*Tarantola et al.*, 2010). The quartz material itself was dry with a water content close to the detection limit of FTIR measurements (*Stünitz et al., 2017*). Most inclusions, especially the larger ones, cracked during the crushing procedure. The crushed material is used to represent a fault gouge. However, during the time at experimental pressure and high temperature, before deformation commenced, the crushed material was effectively hot pressed to a dense coherent crystalline material better termed "cataclasite".

Insert Figure 1 here

The crushed material (0.1 g) with 0.2 wt% water added was introduced between alumina (Al_2O_3) forcing blocks (diameter 6.35 mm), cut at 45° (to achieve maximum shear stress), resulting in a layer of ~1 mm thickness (Fig. 1). The assembly was weld-sealed in a platinum jacket with a nickel foil insert. Sodium chloride was used as confining medium in a Griggs-type solid-medium deformation apparatus (Fig. 1). The temperature was controlled by S-type (Pt/Pt-Rh) thermocouples at T > 800 °C and by K-type (Cr-Al) thermocouples at T ≤ 800 °C. More details on the sample assembly can be found in *Pec* (2014). Samples were pressurised to confining pressure while the temperature was increased in 100 °C steps (at a rate of 20 °C per minute) to experimental conditions. The deformation experiments were started by applying a directional compressive force on the sample, i.e., by moving the σ_1 piston (*Richter et al.*, 2016). The σ_1 piston had to push through a lead piece (so-called run-in) before it touched the alumina forcing block on top of the sample. At this point sample deformation started. When the motor was stopped, the temperature was decreased to 200 °C within 2-3 minutes with cooling rates between 150 °C and 300 °C per minute to quench the microstructure. Five experiments included a hydrostatic hot-pressing stage (at 1000 °C; 1.5-1.6 GPa confining pressure), where the sample was left for 20 hours before decreasing the temperature (2.5 °C per minute) to deformation conditions. These samples will be referred to as ‘hot pressed’.

Two types of experiments were conducted. Experiments of type 1 were conducted at constant displacement rates. The constant displacement rate of the σ_1 piston resulted in an approximately constant shear strain rate. Type 2 experiments are strain-rate stepping experiments, where the displacement rate was decreased by about one half or one order of magnitude after reaching peak strength. When steady state was achieved for this reduced rate the displacement rate was decreased again. During

151 the last step, the displacement rate was set again to the initial value.

152

153 2.2 Mechanical data: acquisition and processing

154 During the experiment, the applied force on the σ_1 piston, the displacement of
155 the σ_1 piston, and the oil pressure of the confining pressure cylinder were recorded
156 with a frequency of 1 Hz. These signals were converted to maximum principal stress
157 (σ_1 in MPa), minimum principal stress (σ_3 in MPa), and axial displacement (d_a in
158 mm). Data processing and determination of differential stress ($\Delta\sigma$), shear stress (τ) and
159 shear strain (γ) were performed according to *Richter et al.* (2016), including a
160 correction for confining pressure build-up and piston overlap. The shear strain (γ) is
161 calculated as the sum of incremental shear strains between recorded data points. For
162 each data point, a reduced width of the shear zone is used by assuming a constant
163 linear thinning of the sample for a known initial average width from hot pressing
164 experiments and final deformed width measured in thin sections.

165 For the determination of the stress exponents and the activation energies, data
166 from the strain rate-stepping experiments and some of the constant shear strain-rate
167 experiments performed at the same deformation temperatures were used. The mean
168 steady-state differential stress and the mean shear strain-rate of each strain-rate step
169 and the differential stress at $\gamma \sim 3$ and the average shear strain rate of the constant
170 shear strain rate experiments were used. The stress corrections of Holyoke and
171 Kronenberg (2010) were not applied because they were not found to be appropriate
172 for the shear experiments in our apparatus (*Richter et al.*, 2017).

173 The friction coefficient of the samples was calculated for the 45° angle of the
174 forcing block pre-cut using a simple Mohr Coulomb construction: $\mu = \tau / \sigma_n$ (Fig. 1b).
175 During deformation, the normal stress on the sample (σ_n) increases (σ_n is calculated as

176 2D mean stress). Steady-state shear stress at γ = 3 was used to calculate the friction
177 coefficient for high strain experiments. For samples only loaded to peak-strength, the
178 maximum friction coefficient was calculated. In the strain rate-stepping experiments,
179 the stress value before decreasing the displacement rate was used for the first step, and
180 for the later strain rate steps the mean values at steady-state conditions were used.
181
182 2.3 Microstructure and texture analysis
183 For the preparation of polished thin sections, the sample jackets were cut
184 parallel to the shear displacement direction and the samples were impregnated under
185 vacuum with epoxy before cutting. For all subsequent microstructural analyses, the
186 samples are viewed with a sinistral shear sense (shear zone boundary is horizontal).
187 All samples were analysed with light microscopy and scanning electron microscopy
188 (SEM; for imaging: a field emission Philips XL 30 ESEM, for electron backscatter
189 diffraction: a field emission Zeiss Merlin SEM with a Nordlys nano camera).
190 Electron backscatter diffraction (EBSD) was used to obtain quartz crystal
191 orientations. Polishing and lapping for EBSD analysis was carried out with colloidal
192 silica suspension Struers OP-U non dry for 3-6 minutes. Samples were coated with a
193 thin carbon layer to prevent charging under high vacuum conditions. Acceleration
194 voltages between 10 kV and 15 kV were used with step sizes of 0.1 to 0.2 µm. EBSD
195 data were measured with AZtec software and analysed with the MTEX toolbox
196 (*Hielscher and Schaeben*, 2008). Initial noise reduction was performed with
197 CHANNEL 5 software by removing isolated points and replacing non-indexed points
198 with the orientation of their neighbours (iteratively filled starting with eight similar
199 neighbours down to six or five similar neigbours).
200 Grain maps obtained with MTEX show individual grains separated by a

misorientation angle of 10°. Dauphine twin boundaries (misorientation of 60 ± 5°) were not considered grain boundaries. Grains had to contain at least five pixels to be considered as grains. The 2D grain diameters (d_{equ} = diameter of area equivalent circle) were used as input for the StripStar programme (*Heilbronner and Barrett*, 2014) to obtain the 3D diameters (D_{equ} = diameter of the volume equivalent spheres). The volume weighted distributions of D_{equ} were fitted with a Gaussian Normal, the modal value and the dispersion being given by the mean and the standard deviation. For details on segmentation and grain size determination, see *Heilbronner and Kilian* (2017).

The kernel average misorientation of a grain (gKAM) is calculated from noise reduced EBSD data with a kernel of an order of 4 (see *Kilian and Heilbronner*, 2017). The 'mis2mean' value of each point of a grain is determined with MTEX. Averaging the 'mis2mean' value of a single grain yields the grain orientation spread (GOS). The GOS is normalised for the long axis (GOS_{la}) to account for the grain-size dependence, which is especially pronounced for highly elongated grains. Both, GOS_{la} and gKAM, indicate the misorientation density of a grain and are therefore considered a measure for intragranular deformation (for derivations of GOS, see *Cross et al.*, 2017).

Using smoothed grain boundaries, the PARIS factor, a measure for grain boundary lobateness (*Panozzo and Hürlimann*, 1983) is used. It is defined by the difference between the length of the convex hull of a grain and that of the real perimeter.

3. Mechanical results

27 constant shear strain-rate experiments between 500 °C and 1000 °C (Table 1) and five strain rate-stepping experiments at shear strain rates between ~2.5 x 10^{-6} s^{-}

^{1} and ~2.5 x 10^{-3} s^{-1} for ~650 °C, 800 °C, 900 °C and 1000 °C (Table 2) were conducted.

Insert Table 1 and 2 here

3.1 Temperature dependence

Above temperatures of ~650 °C, samples clearly weaken systematically with increasing temperature, whereas at 650 °C and below, the strength-temperature-relationship is weak or unsystematic (Fig. 2a). Samples deformed at temperatures below 700 °C show steady-state behaviour or slight strain hardening. At 700 °C or higher, the samples deform below the Goetze criterion ($\Delta\sigma = P_c$) and show steady-state or minor strain weakening at high strain. The difference in strength between 650 °C and 700 °C is very large (~1300 MPa). At low temperatures, no significant stress drop or strain weakening occur after yield strength, except for 450br and 481br (see Table 1). These samples show a stress drop as a result of slip along the forcing block. In addition, the alumina forcing blocks started to deform because of the high stresses (e.g., 415br).

The slopes of the loading curves up to temperatures of 650 °C are almost identical up to a differential stress of ~1 GPa. At temperatures above 650 °C the slope decreases with decreasing strength and shear strain rate (Figs. 2, 3 and 4).

Insert Figure 2 here

3.2 Pressure dependence

At 650 ºC, the sample strength increases with increasing confining pressure, whereas at higher temperatures (700 °C and 800 ºC; Fig. 3) strength decreases with increasing confining pressure. At 800 ºC, a pressure dependence is not obvious

between 1.0 and 1.5 GPa, but between 0.5 and 1.0 GPa, the weakening with increasing confining pressure is very clear (Fig. 3).

Insert Figure 3 here

3.3 Influence of initial grain size

When hot pressed at 1000 °C for 20 hours prior to deformation, samples systematically reach higher strengths compared to samples without hot pressing (Fig. 2c). The difference in flow stress is at least 500 MPa at 600 °C at $\gamma \sim 3$ (the forcing blocks start to deform in the hot-pressed sample at such high stresses). At 700 °C, the hot-pressed sample is about 900 MPa stronger and shows strain hardening, whereas the non-hot pressed sample weakens. At 800 °C, the difference is ~200 MPa and both samples show strain weakening.

One sample with a small initial grain-size fraction (7-11 µm) is deformed at 1.5 GPa, 800 °C and $2.5 \cdot 10^{-5}$ s^{-1} (Fig. 2c, 445br). It is weaker than the experiments with a larger initial grain-size fraction (< 100 µm) performed at the same strain rate and temperature conditions. At $\gamma \sim 3$, the differential stress of 445br is less than half as high as of 388br (difference ~500 MPa). Steady-state conditions exist between a shear strain of ~0.5 to 2.5, after that the sample hardens by ~100 MPa until the end of the experiment.

3.4 Strain rate dependence

Strain rate has a pronounced effect on sample strength at temperatures above 600 °C. At 650 °C and 800 °C, increasing the strain rate by one order of magnitude shifts the flow stress from below to above the Goetze criterion (Fig. 2b). At 900 °C the same shift is achieved by increasing the strain rate by two orders of magnitude.

Strain rate-stepping experiments in combination with constant displacement experiments at different rates show distinct strain rate dependence for all higher temperature experiments, except at 650 °C, where the rate dependence is only observed at very low strain rates (~$10^{-6}s^{-1}$; Fig. 4). The fastest strain rate causes the highest stresses, and lower stresses with increasing temperature and lower strain rate occur at all strain rates (Fig. 4). The strain-rate-stepping tests are plotted together with constant strain-rate tests to check the reproducibility of the results. At 900 °C and 1000 °C, the last step has slightly higher shear strain-rates than the first step (because of the thinning of the shear zone), and therefore, the differential stress is slightly higher. The experiment at 900 °C shows abrupt strain hardening at the end of the last strain rate step. This behaviour is a consequence of the sample geometry where the lower forcing block collided with the upper alumina piston. At 800 °C, the experiment failed at the slowest strain rate step.

Insert Figure 4 here

One strain-rate-stepping experiment included a hot-pressing stage prior to deformation (480br). The initial sample strength is similar to that of the hot-pressed constant-displacement experiment (419br, Fig. 4). At lower strain rates, the stresses of the hot-pressed sample are similar the sample 388br without hot pressing. At the end of the experiment, the strain-stepping sample (480br) is 200 MPa weaker than the constant rate sample (419br).

4. Microstructural observations

The brittle and the viscous microstructures are described in terms of being discrete Riedel surfaces without discernible shear displacement and a synthetic low-angle orientation (R) or an antithetic high-angle orientation (R´) with respect to the

shear plane are termed "Riedel surfaces". When such features have a discernible width, they are termed "shear bands" (SB, not distinguishing C or C´ orientations in the sense of *Berthé et al.* (1979)). Riedel surfaces and shear bands may occur in the same sample. Elongated quartz grains or grain aggregates typically develop a shape preferred orientation, which is termed "foliation" (F) here.

4.1 Starting material

From analyses with a laser diffraction particle size analyzer, we know that the crushed quartz powder initially has a fractal size distribution with a fractal dimension of 2.4 in the size range up to 100 µm. During the run-in of the σ_1-piston, before the piston touches the forcing block, the samples are exposed to varying periods (up to 25 hours) of hydrostatic heat treatment. During this time, the same kind of grain growth takes place as in the healing faults described by Keulen et al. (2008), so that the grain-size fraction <1 µm disappears (Fig. 5). Grain growth creates a normal distribution of grains at the lower size end of the fractal distribution.

A few samples were additionally hot pressed after reaching experimental conditions (20h at 1000°C). After 25 h and 800°C, the 3D mode of the grain size fraction <30 µm is ~9.1 µm, and after 20 h at 1000 °C, it is ~12.8 µm (Table 3). The initial gouge material is now fully compacted and fully cohesive. For the higher temperature samples (700 °C to 1000 °C), porosity is < 1%, whereas for lower temperature samples (500 to 600°C) porosity is up to ~10 % (values obtained from image analysis) due to a lack of grain growth.

Insert Figure 5 here

Insert Table 3 here

4.2 Deformation microstructures

Low-temperature samples (T ≤ 650°C) are dominated by a complex Riedel surface geometry with synthetic R and rare antithetic R' surfaces (Fig. 6; samples 450br, 479br, 415br, 435br). The R surfaces form at an angle of 20-30° to the direction of the applied load (σ_1- direction) and have a predominantly brittle appearance at 500°C. The R surfaces are not connected and never transect the whole sample. These observations, in conjunction with the mechanical data, indicate that these R surfaces do not fully control the sample strength. Most original clasts are still visible but have rounded edges and corners. Undulatory extinction and discrete surfaces with small misorientation and with a high angle towards the shear zone boundary exist in several clasts at 650°C (Fig. 6; sample 435br). Tails at clasts are partly developed without resolvable small particles at the light or scanning electron microscope scale at 650°C. Deformation lamellae start to develop in clasts at 600 °C. Shear bands are developed at 650 °C in addition to the R surfaces. At 600 °C, zones with small, equi-axed grains evolve in R surface orientation. These zones become more pronounced at higher temperatures, defining shear bands (Fig. 6; samples 479br, 435br, 493br, 419br).

Insert Figure 6 here

At higher temperatures (T ≥ 700 °C), viscous processes dominate the microstructure (Fig. 6; samples 383br, 388br, 412br, 493br, 419br). At 700 °C and 800 °C, a shear band and foliation fabric is developed (Figs. 6, 7; samples 383br, 388br, 412br, 493br, 419br, 452br, 447br, 448br, 499br), and Riedel surfaces are absent. Elongated tails of recrystallized grains develop at rounded clasts. With increasing shear strain and higher temperature, the shear band and foliation fabric evolves into a single penetrative foliation of elongated clasts and recrystallised grains.

Large clasts show more penetrative recrystallisation with increasing temperature of deformation and with increasing strain. At γ ~5 about 10 % clasts remain at 700 °C and 5 % clasts can be distinguished at 800 °C (Fig. 6; samples 383br, 493br, 388br). Rounded clasts are predominant at 700 °C. At 800 °C, highly elongated aggregates of recrystallised grains dominate. Deformation lamellae are pronounced in clasts at 700 °C and 800 °C, but rare at 900 °C. At 900 °C and 1000 °C, the elongated aggregates of recrystallised grains give way to a more homogeneous groundmass of recrystallised grains with some clasts preserved in the recrystallised matrix (Fig. 6; samples 412br, 337br).

In samples with hot pressing (20h at 1000°C), pre-existing cracks are anneal and barely visible. Subsequent deformation at 600 °C does not produce an obvious brittle deformation fabric of the sample (Fig. 6; sample 415br). No Riedel surfaces develop and only minor grain-boundary alignment occurs. At 700 °C and high strains, a shear band and foliation fabric is present with several remaining rounded clasts that develop tails (Fig. 6; samples 493br). At a given shear strain, the foliation angle with the shear zone boundary is clearly larger than in samples without hot pressing and the microstructure appears less deformed. At 800 °C, a pervasive foliation dominates the fabric, again with a slightly larger angle after similar shear strain than in the hot pressed sample (Fig. 6; sample 483br). More or less elongated clasts are present compared to the sample without hot pressing.

4.3 Effect of strain rate on microstructure

Three constant shear strain-rate experiments were conducted at shear strain rates different from ~$2.5 \cdot 10^{-5}$ s^{-1} (Fig. 2b). At 650 °C and a shear strain rate of $0.35 \cdot 10^{-5}$ s^{-1} several grains show more brittle deformation, and less rounded grain

shapes at low shear strain (γ = 1.1; Fig. 7; sample 500br). Shear bands are absent and the fabric resembles samples deformed at lower temperatures at 2.5 x 10^{-5} s^{-1} (Fig. 6; sample 479br). At 800 °C and 900 °C, faster shear strain rates ($27 \cdot 10^{-5}$ s^{-1} and $189 \cdot 10^{-5}$ s^{-1}, respectively) cause a more heterogeneous deformation, shear bands, and samples resemble those deformed at ~100 to 200 °C lower temperatures at strain rats of 2.5 x 10^{-5} s^{-1} (Fig. 7; samples 447br, 499br).

Insert Figure 7 here

4.4 Effect of confining pressure on microstructure

Samples deformed at 1.0 GPa confining pressure and 650 °C show Riedel surfaces and less commonly shear bands, very similar to samples deformed at 1.5 GPa confining pressure (Figs. 6, 7; samples 494, 435br). Clast shapes are less rounded than at 1.5 GPa confining pressure (cf. Figs. 6 and 7, shear strain is higher in Fig. 7; samples 494br, 435br). At 700 °C, 1.0 GPa, the samples are characterised by a larger number of shear bands and less homogeneous deformation than at 1.5 GPa (cf. Figs. 6 and 7; samples 494br, 435br), whereas at 800 °C, 1.0 GPa, more clasts survive and the recrystallisation is less complete than at 1.5 GPa (cf. Figs. 6 and 7; samples 448br, 388br).

At 0.5 GPa confining pressure and 800 °C, deformation is localised in long synthetic R surfaces accompanied by several transgranular fractures (Fig. 8; sample 386br). Most of the displacement is accumulated along the R surfaces, where the gouge material is highly pulverised (submicron-scale) (Fig. 8b). Large clasts are slightly rounded at the edges (Fig. 8a) and microstructures resemble those of the 650°C, 1.5 GPa sample (cf. Fig. 6; sample 435br). In the series of 0.5, 1.0, and 1.5 GPa samples, more brittle deformation microstructures clearly develop with

401 decreasing confining pressure, particularly toward the lower pressure end.

402 **Insert Figure 8 here**

403

404 4.5 Grain size

405 At conditions of 1.5 GPa confining pressure and shear strain rates of ~$3 \cdot 10^{-5}$ s^{-1}
406 , the 3D mode of recrystallized grain size increases from 2.1 µm at 700 °C to >15 µm
407 at 1000 °C (Fig. 9a, Table 3). The sample that was prepared with a grain-size fraction
408 of 7-10 µm, yields a slightly larger grain size of 4.4 µm compared to the standard
409 sample that yields 4.1 µm at the same temperature (800°) (Fig. 9b). At 1.0 GPa
410 confining pressure, the recrystallised grain size is slightly smaller than at 1.5 GPa (1.5
411 versus 2.1 µm at 700 °C, and 3.3 versus 4.1 µm at 800°C). At 0.5 GPa and 800 °C, no
412 recrystallization occurs. Shear strain rates faster than the standard value of $3 \cdot 10^{-5}$ s^{-1}
413 cause smaller recrystallised grain sizes. At 800 °C and 10 times faster, the 3D mode is
414 2.0 µm versus 4.1 µm, at 900 °C and 100 times faster, it is 1.5 µm versus 6.1 µm
415 (Table 3).

416 **Insert Figure 9 here**

417 An initial hot-pressing stage causes growth of the small grains (Fig. 5, Table 3)
418 and the resulting grain sizes at the onset of deformation are larger. After deformation,
419 the recrystallized grain size of these samples is similar to that of samples without hot
420 pressing (1.6 µm compared to 2.1 µm at 700 °C, 4.8 µm compared to 4.1 µm at 800
421 °C; cf. Fig. 9b, Table 3).

422

423 4.6 Texture

424 The values of GOS and gKAM, indicators of intragranular deformation,
425 decrease with increasing temperature between 700 °C and 1000 °C (Fig. 10) with hot

426 pressed samples showing similar values to samples without hot pressing. For
427 individual grains, neither PARIS factors, indicating high lobateness, nor grain size
428 correlate with GOS and gKAM values.

429 **Insert Figure 10 here**

430 Above 650 °C, the recrystallised matrix dominates the CPO for standard
431 confining pressure (1.5 GPa) and standard shear strain rates (~$2.5 \cdot 10^{-5}$ s^{-1}). Separate
432 pole figures are calculated for smaller and larger fractions of recrystallized grains
433 (Fig. 11). The delimiting size between small and large grains is derived from the 3D
434 mode of the size distribution of recrystallized grains (< 25 µm; Fig. 11). Pole figures
435 are calculated for grains with 2D diameters (= area equivalent diameters) larger or
436 smaller than the delimiting 3D diameter, i.e., pole figures for grains larger than the 3D
437 mode and pole figures for grains predominantly smaller than the 3D mode. For the
438 larger grain size fraction, the CPO is always considerably stronger. The CPO
439 progressively evolves between 700 °C and 1000 °C. At 700 °C and 800 °C, there is
440 one peripheral maximum of the *c*-axes slightly rotated with the sense of shear. At 900
441 °C, a peripheral and a central *c*-axis maximum both are established. Towards 1000 °C
442 the CPO evolves to a single central *c*-axes maximum.

443 The pole figures of the fine-grained fraction shows a different development
444 with increasing temperature. At 700°C, the CPO is more diffuse and the peripheral *c*-
445 axis maximum is less pronounced compared to that of the larger grain size. The
446 orientation of the maximum is similar to the maximum of the larger grains. At 800 °C,
447 the smaller grains (< 4 µm) again show a more diffuse CPO, but the *c*-axis maximum
448 is rotated by 20° with the sense of shear with respect to that of the larger grains. At
449 900 °C, the peripheral c-axes are more dispersed and the c-axis maximum is rotated
450 by 10° with the sense of shear compared to that of the larger grains. The central

451 maximum of *c*-axes is less pronounced than that of the larger grains. The central c-
452 axis maximum at 1000 °C is present in fine grains as well as in larger grains. A
453 rotation with the sense of shear cannot be identified.

454 **Insert Figure 11 here**

455

456 5. Discussion

457 Our series of experiments employs crushed material of natural quartz. This
458 approach simulates a cataclasite produced by brittle deformation in nature such as
459 seismic or aseismic movement along a fault. Such a cataclastic rock deforms
460 dominantly by frictional mechanisms at low temperatures, high strain rates and low
461 confining pressures, and by fully viscous mechanisms at higher temperatures, lower
462 strain rates and higher confining pressures. The differences in the mechanical data and
463 microstructures demonstrate that the starting material used here is adequate to study
464 the brittle-to-viscous transition (BVT) as a function of pressure, temperature and
465 strain rate in polycrystalline quartz rocks. Another aspect that may be studied by using
466 such a material is how deformation mechanisms change as a function of deformation
467 history, i.e. from a brittle precursor material to a subsequently viscously deformed
468 material. Such a transition may occur, e.g., as a transition from seismic to postseismic
469 creep.

470

471 5.1 Mechanical parameters of the brittle-to-viscous transition

472 The BVT can be defined on the basis of different parameters: mechanical data
473 with respect to the Goetze criterion ($\Delta\sigma \approx P_c$); pressure dependence of differential
474 stress; friction coefficients and stress exponents, and microstructural transition from
475 dominantly brittle to viscous deformation structures.

The greatest difference in differential stress at a strain rate of ~10^{-5} s^{-1} is observed between the 600/650 °C and 700 °C samples (Fig. 2a) where the strengths lie above and below the Goetze criterion that marks the transition from brittle ($\Delta\sigma > P_c$) to viscous ($\Delta\sigma < P_c$) deformation ("plastic" in *Kohlstedt et al.*, 1995). This observation places the BVT between 650 °C and 700 °C for a strain rate of ~10^{-5} s^{-1} in terms of the Goetze criterion.

For experiments by others at the same axial strain rates as our shear strain rates (*Hirth and Tullis*, 1994), the strength of quartzite samples at 700 °C and 850 °C (at P_c =1.2 GPa) shows substantial scatter, but similar average values as our samples. The deformation processes in that study were identified as semi-brittle flow (700 °C) and dislocation creep (850 °C). The similar sample strengths of the intact rock and our gouge material indicate that at higher temperatures the cataclasite is fully compacted and behaves like a normal polycrystalline material. We attribute the temperature differences for the BVT between our samples and those of *Hirth and Tullis* (1994) to differences in the amount of total strain attained and that samples in shear are weaker than in axial compression, so that localisation in coaxially deformed samples occurs in narrower zones than in our shear zones, causing greater strain rates.

The BVT coincides with another mechanical observation in the samples: At stresses below the Goetze criterion, the slope of the loading part of the stress strain curves decreases systematically with decreasing flow stress (Figs. 2, 3 and 4). The loading curve in the Griggs apparatus is not purely elastic at higher temperatures. The systematically decreasing slope at higher temperatures is the result of increasing viscous deformation processes in the samples during loading. In experiments deformed above the Goetze criterion, the slope is similar for all samples, indicating no substantial viscous deformation processes during loading.

Higher confining pressures cause greater sample strength for frictional sliding (*Byerlee*, 1978) and cracking (*Paterson and Wong*, 2005 and references within), whereas the viscous creep strength of wet quartz decreases with increasing confining pressure (*Tullis et al.*, 1979; *Kronenberg and Tullis*, 1984). The observed strengthening of samples with increasing pressure at low temperatures (650 °C, Fig. 3) is consistent with frictional or brittle behaviour (cf. Hirth and Tullis, 1994). The lowering of flow-stress with increasing pressure observed at $T > 650$ °C (Fig. 3) indicates the onset of viscous deformation. At a first glance, the difference in flow stress between samples deformed at 1.0 and 1.5 GPa P_c (453br and 437br) does not appear significant (Fig. 3), but when seen with respect to the Goetze criterion, the difference is well defined: The sample at 1.5 GPa (437br) barely reaches the Goetze criterion, whereas the sample at 1.0 GPa (453br) is clearly above it. The difference in flow stress is clearly established at low P_c between 0.5 GPa and 1.0 GPa (Fig. 3). A very similar trend was observed in novaculite by *Kronenberg and Tullis* (1984): a smaller stress dependence at $P_c \geq 1.0$ GPa and a distinct pressure dependence at lower confining pressures. The decreasing peak stress with increasing pressure is related to increased water fugacity and its enhancing effect on crystal plasticity (*Tullis et al.*, 1979; *Kronenberg and Tullis*, 1984; *Paterson and Luan*, 1990; *Kohlstedt et al.*, 1995). The pressure dependence delineates the BVT also in the range of 650 °C to 700 °C for ~10^{-5} s^{-1}.

5.2 Coefficient of friction

To delineate the BVT better, mechanical properties such as friction coefficient and stress exponent can be used. Frictional deformation should be rather temperature insensitive up to 440 to 500 °C (*Paterson and Wong*, 2005, p. 172), whereas viscous

526 deformation is by definition temperature dependent. Viscous flow laws imply a strong
527 positive stress dependence for the strain rate (*Orowan*, 1940; *Kohlstedt and Hansen*,
528 2015), whereas in frictional deformation the strain rate at slow sliding rates (as
529 employed in this study) are assumed to be weakly dependent or strain-rate
530 independent as a first approximation (*Byerlee*, 1978; *Kohlstedt et al.*, 1995; *Paterson*
531 *and Wong*, 2005, p. 178, and references therein). To better use the mechanical data for
532 defining the BVT, we determined the friction coefficients and stress exponents for
533 many of our experiments, even if these mechanical properties are outside the range of
534 conditions for which brittle deformation would be expected.

535 At 1.5 GPa and below 700 °C, the friction coefficient (μ ~ 0.45; Fig. 12) is
536 somewhat less than normal rock friction values (0.6; Byerlee, 1978). The temperature
537 dependence is very small up to 650 °C. From 700 °C to 1000 °C, the friction
538 coefficient shows a systematic temperature dependence. At 1.5 GPa confining
539 pressure and a strain rate of $2.5 \cdot 10^{-5}$ s^{-1}, the friction coefficient μ ~ 0.3 to 0.05, at a
540 strain rate of $2.5 \cdot 10^{-4}$ s^{-1}, μ ~ 0.35 to 0.16. At strain rates of ~10^{-6} s^{-1}, the friction
541 coefficients become very small (μ < 0.02). Low confining pressures cause greater
542 friction coefficients between 650 °C and 800 °C (Fig. 12b): At 0.5 GPa and 800 °C,
543 the greatest friction coefficient occurs (μ = 0.53), which is twice the value at 1.0 GPa.
544 A distinct jump in the values occurs for the friction coefficient between 650 °C and
545 700 °C for a strain rate of 2.5 x 10^{-5} s^{-1}, coinciding with the Goetze criterion (Fig. 12).

546 **Insert Figure 12 here**

547 Frictional deformation in quartz and granite, in general, is only weakly
548 temperature-dependent below 350-400 °C (*Blanpied et al.*, 1995; *Chester and Higgs*,
549 1992), so that the smaller friction coefficients and the strong temperature dependence
550 at T > 650 °C also indicate a change in deformation mechanism to viscous behaviour.

The pronounced strain rate dependence of strength between 650 °C and 900 °C (Figs. 2b, 4, 12a) is present down to temperatures as low as 650 °C (Fig. 4). This behaviour emphasises the contribution of viscous deformation processes, and thus a semi-brittle character at these low temperatures. It is remarkable that in one sample (500br) at temperatures of 650 °C, the flow stress can be below the Goetze criterion. However, in that sample, steady state was not achieved because at the low strain rate of ~10^{-6} s^{-1} only a small total strain was attained (Figs. 2b and 4). Strain rates of ~10^{-4} s^{-1} are required to achieve sample strengths above the Goetze criterion and realistic friction coefficients at T = 800 °C, whereas a strain rate of ~10^{-3} s^{-1} is required at T = 900 °C (Figs. 2b, 12a). These results can be used to extrapolate the BVT to lesser strain rates (see below).

5.3 Stress exponent and activation energy

Based on a power-law creep relationship, the stress and strain rate data can be used to derive a stress exponent and an activation energy (Fig. 13):

$$\dot{\gamma} = A \cdot \Delta\sigma^{n} \cdot \exp^{-\frac{Q}{R \cdot T}} \qquad \text{(Eq. 1)}$$

where $\dot{\gamma}$ [s^{-1}] is the shear strain rate, A [$MPa^{-n} \cdot s^{-1}$] is a material-dependent constant, $\Delta\sigma$ [MPa] is the differential stress, n is the stress exponent, Q [J/mol] is the activation energy, R [$J \cdot mol^{-1} \cdot K^{-1}$] is the ideal gas constant and T [K] is the temperature. At low temperatures (~650 °C), the n-value is high (n = 6.4 ± 1.3). The stress exponent of high-temperature experiments (800-1000 °C) is 1.9 ± 0.6 (Fig. 13a) and shows little variation with temperature. For high temperature experiments, the activation energy is determined to be ~170 ± 72 kJ/mol (Fig. 13b).

The highest stress values at 900 °C (499br at ~10^{-3} s^{-1}) and 800 °C (447br, fast step of 488br at ~10^{-4} s^{-1}; Fig. 4) are not included in the determination of the stress exponent

and the activation energy because steady state is not indicated by the mechanical data.

Insert Figure 13 here

The calculated stress exponents confirm the transition from brittle-dominated to viscous-dominated deformation at temperatures of 650 / 700 °C, and strain rates of ~10^{-5} s^{-1}. The stress exponent of ~6.4 of samples deformed at low temperatures (Fig. 13) is too high for dislocation creep deformation with typical values of n = 3-5 (e.g., *Karato*, 2008; *Paterson*, 2013; *Kohlstedt and Hansen*, 2015), thus indicating the beginning of the power-law breakdown, i.e., the lack of rate-controlling viscous deformation at T < 700 °C. On the other hand, the *n*-values of 1.8 to 2 derived for samples deformed at T > 700 °C (Fig. 13) are too low for dislocation creep, yet rather high for diffusion creep.

Our determined Q-value of 168 to 170 kJ/mole is very similar to values determined by *Jaoul et al.* (1984) and lies in the range of other experimentally determined values for dislocation creep (Table 4). Activation energies for diffusion creep vary considerably and the values are highly dependent on the involved material (silicon or oxygen diffusion) and the controlling process (transport or reaction) (e.g., 137-178 kJ/mol for silicon diffusion in *Farver and Yund*, 2000; 142-243 kJ/mol for oxygen diffusion in *Giletti and Yund*, 1984; 220 kJ/mol in *Rutter and Brodie*, 2004a). Hence, the range of previously determined activation energies and the precision of our determination are inadequate to conclude decisively about the nature of the process causing it. Rutter and Brodie, 2004a,b are the only studies that have determined activation energies for both processes, and the values are very similar (Table 4). Based on this evidence and our observations of a constant stress exponent of n ~2 between 800 °C to 1000°C, we would like to maintain the idea that the activation energies of contributing diffusion creep and dislocation creep mechanisms should be similar.

Insert Table 4 here

A stress exponent ($n \sim 2$) has been derived for deformation by dislocation-accommodated grain-boundary sliding by, e.g., *Kohlstedt and Hansen* (2015). However, the rather strong CPOs occurring in our samples argue against grain boundary sliding (GBS). Although evidence exists for strong CPOs produced by GBS (e.g., *Schmid et al.*, 1987; *Gomez Barreiro et al.*, 2007; *Hansen et al.*, 2011), the general consensus is that dominant GBS should produce weak CPOs (e.g., *Edington et al.*, 1976; *Bell and Langdon*, 1967). A possible explanation is a combination of deformation processes, where dislocation creep produced strong CPOs and *n*-values of 3 to 5, in tandem with grain-size-sensitive diffusion creep, including grain boundary sliding, which produced weak CPOs. Both together yield *n*-values of ~2.

To derive a grain-size exponent, we used samples 388br (standard), 419 (hot pressed) and 445br (sieved to 7-11µm), which were all deformed at 800 °C, 1.5 GPa and 10^{-5} s^{-1}, but yielded significantly different differential stresses. The grain size exponent $p = m / n$, where m is the slope of the linear fit in the log(stress) versus log(grain size) diagram (Fig. 13c) and n is the average stress exponent of 1.9. The correlation coefficient for this fit is very low (R=0.258), and the value of p = 1.08 is not well constrained. While our database is far too small for a reliable determination of the grain size exponent, it is nevertheless interesting to note that similar uncertainty is present in published data (Rutter and Brodie, 2004a).

5.4 Microstructure development at the brittle-to-viscous transition

The microstructural changes correspond to the transition conditions inferred from the mechanical data. At strain rates of ~10^{-5} s^{-1}, the samples at $T \geq 700$ °C show features of dynamic recrystallisation, whereas at lower temperatures, Riedel fractures

626 across grains are common (Figs. 6 and 7). The transition between brittle and viscous
627 microstructures is clearly visible between 650 °C and 700 °C at the strain rate of ~10^{-5}
628 s^{-1} and confining pressures of 1.0 and 1.5 GPa. This observation is in excellent
629 agreement with the transition defined by mechanical data discussed above. The effect
630 of confining pressure becomes obvious in the microstructures at low confining
631 pressure of 0.5 GPa, where samples at 800 °C show predominantly brittle
632 microstructures (Fig. 8). The strain rate effect is not as clearly expressed in the
633 microstructure: At 650 °C, deformation at a strain rate of ~10^{-6} s^{-1} produces similar
634 microstructures as a strain rate of ~10^{-5} s^{-1} (cf. Figs. 6, 7). But at ~10^{-5} s^{-1}, clasts are
635 more rounded, and Riedel surfaces and shear bands are more pronounced. These
636 differences may well be due to the less total strain of the sample for a slower strain
637 rate. The faster strain rates at 800 °C and 900 °C yield microstructures that resemble a
638 mixture of microstructures at a strain rate of ~10^{-5} s^{-1} between 600 °C and 700 °C (for
639 high shear strain): several remaining large clasts coexist with clusters of recrystallised
640 grains in a fabric dominated by shear bands (below referred to as “transitional”).
641 At stresses above the Goetze criterion, typical regime 1 stress-strain curves
642 with pronounced weakening after peak stress (*Hirth and Tullis* (1992) are only
643 observed at 800 °C and a strain rate of ~$2.5 \cdot 10^{-4}$ s^{-1} (Fig. 2). Bulging recrystallisation
644 concentrates along shear bands producing small new grains. After sufficient
645 recrystallisation, strain partitioning and weakening occur while mechanical and
646 microstructural steady state are not achieved. Below the Goetze criterion, generally at
647 higher temperatures and slower strain rates, minor strain weakening occurs, except at
648 1000 °C where steady state is attained (Fig. 2). The associated microstructure is
649 dominated by a pervasive shape foliation of recrystallised grains and the development
650 of a CPO. Hence, mechanical steady state is approached, but not perfectly realised,

and this result is consistent with incomplete recrystallisation (Fig. 6), a switch from one deformation mechanism to the next, or simultaneous operation of two mechanisms.

5.5 Texture and grain size at the brittle-to-viscous transition

5.5.1 Misorientation density

So as to distinguish recrystallised grains from potential survivor grains of the original quartz material on the basis of some intragranular misorientation density, the grain kernel average misorientation (gKAM) and the grain orientation spread normalised with respect to the long axis (GOS_{la}) were measured. We initially assumed that low intragranular misorientation densities are characteristic of newly recrystallised, recovered grains, whereas high misorientation densities are typical for the original crushed material. However, it was found that recrystallising grains continue to accumulate intragranular strain as the overall shear deformation continues. Accordingly, the gKAM remains high and rather reflects grain-scale strain (*Kilian and Heilbronner*, 2017). A correlation of high gKAM with small (recrystallized) grain size has also been noted (*Heilbronner and Kilian*, 2017). In other words, the gKAM, or any other measure of internal misorientation density, does not reflect recovery, and therefore cannot be used to distinguish recrystallized grains from relict grains.

However, gKAM and GOS_{la} do vary as a function of temperature: The higher the deformation temperature, the smaller the intragranular misorientation density (Fig. 10). Pre-deformation hot pressing or sieving does not significantly influence this trend. At lower temperatures, large grains with high PARIS factors (more lobate grains) have higher gKAM and GOS_{la} values than the small grains with low PARIS factor (fully convex grains). In other words, large grains tend to have high

misorientation densities while small grains display the full spectrum of misorientation density, from fully recovered to highly strained. This distinction becomes progressively smaller with increasing temperature, until, at 1000 °C, all grains, irrespective of shape and size, have very small misorientation densities, i.e., appear fully recovered.

5.5.2 CPO of diffusion and dislocation creep

To investigate if diffusion creep and dislocation creep are grain-size selective, we consider the textures of the small and the large grain-size fractions separately (Fig. 11). Small and large grain-size fractions are delimited by the 3D mode which as a result the number of grains in the smaller and larger fraction differ considerably. Pole figures are therefore weighted by the area of the evaluated grains to avoid artefacts. We also checked by comparing number-weighted pole figures that were calculated for the large grain-size fraction and for the same number of randomly selected small grains. The texture indices and the pole figure maxima of [*c*], <*a*>, and <*r*> pole figures of smaller grains are weaker than those for larger grains. The weaker textures are consistent with diffusion creep mechanisms being active in the smaller grain size fraction.

At 700 °C, the weaker texture of the small grains is attributed to processes such as solution precipitation and nucleation. At 800 °C and 900 °C, textures of the small grains are not only weakened but also the c-axis maxima are rotated with respect to those of the large grains. For 800 °C and 900 °C, the rotation is 20° and 10°, respectively, clockwise in the sense of the applied shear, compatible with grain-boundary sliding and a stiff rotation of grains. At 1000 °C, the difference between the pole figures of the smaller and larger grain size fractions is the texture strength, not in the texture type. As the rotation axis of the applied shear is parallel to the (strong) *c*-

axis maximum, a potential rotation is difficult to discern.

Comparing the experimental quartz deformation analysed here with results derived from naturally or experimentally deformed quartzites, we find that the CPO evolution of the larger grain-size fraction (Fig. 11) is consistent with observations where high temperature deformation produces a central *c*-axis maximum, whereas low temperature deformation (or small shear strains in experiments) produces peripheral maxima (e.g., *Schmid and Casey*, 1986; *Stipp et al.*, 2002; *Heilbronner and Tullis*, 2002, 2006). In terms of the three microstructural regimes identified in nature, the 700 °C and the 800 °C experiments would coincide with BLG (bulging), the 900 °C sample with SGR (subgrain rotation) and the 1000°C sample with GBM (grain boundary migration). In a more recent study by *Kilian and Heilbronner* (2017), it was found that the textures of Black Hills quartzite (BHQ) deformed in the dislocation creep regimes 1, 2, and 3, develop from a peripheral *c*-axis maximum towards a central *c*-axis maximum as the result of a transition from dominant nucleation / bulging recrystallisation to dominant subgrain rotation recrystallisation.

5.5.3 Grain size distributions in diffusion and dislocation creep

In a mixed mode of diffusion creep and dislocation creep, as inferred here from the stress exponents of $n \sim 2$, diffusion creep is expected to be more efficient in small grains while dislocation creep, which is grain-size insensitive, should be more active in larger grains (*Tullis*, 2002). An estimate for the upper grain-size limit of grain-size-sensitive creep is given as <1 µm (*Rutter and Brodie*, 2004a), whereas *Luan and Paterson* (1992) estimate the upper size limit to be ~20µm. The recrystallised grain size measured for our experiments at T = 800 - 1000 °C, is well within these limits: Recrystallised grain sizes range from <1 µm up to 25 µm, with modal values (3D mode) of ~4, ~6 and ~10 µm for 800 °C, 900 °C and 1000°C, respectively (Fig.

726 9). As was shown, the partitioning of deformation mechanisms into smaller and larger
727 grain size fractions takes place in our samples for grain size below and above these
728 modal values as a threshold. Our threshold values are closer to the transition limit of
729 Luan and Paterson (1992) for dislocation and diffusion creep.

730 Before reaching the hit point, the original fractal grain-size distribution has
731 been modified by grain growth. We can estimate from the analysis of two hot-
732 pressed samples that the very smallest size fraction has been obliterated in a manner
733 described by Keulen et al. (2008) for healed faults. However, we do not know how
734 far grain growth proceeded during pressurization and heating, and what the smallest
735 grain size may be at the start of the experiment. In contrast, when the starting
736 material consists of a grain-size fraction of 7-11 µm (sample 445br), we know that
737 any grain smaller than 7 µm must have formed during deformation, possibly by a
738 process such as bulging recrystallisation, nucleation (*Kilian and Heilbronner*, 2017),
739 or creep cavitation (*Precigout and Stunitz*, 2016). Comparing samples 445br
740 (sieved), 388br (standard) and 419br (hot pressed), we note that the grain sizes and
741 stress do not follow a piezometric relation. Grain sizes (3D modes) of 4.4, 4.1 and
742 4.8 µm were measured for flow stresses of 309, 791 and 1016 MPa, respectively.
743 Rather than decreasing with grain size, stress seems to increase (cf. Fig. 13c). In
744 other words, the piezometer relation does not hold and pure dislocation creep can be
745 excluded, suggesting that a substantial contribution of diffusion creep has to be
746 inferred.

747

748 5.6 Using the Griggs apparatus for the derivation of stress exponents

749 As mentioned above, for dislocation creep in quartz, stress exponents of n = 3-
750 5 are often given in the literature (*Gleason and Tullis*, 1995; *Luan and Paterson*,

751 1992, *Hirth et al.*, 2001), despite the fact that lower values were determined
752 experimentally ($n \leq 2.5$) in many cases (e.g., *Jaoul et al.*, 1984; *Kronenberg and*
753 *Tullis*, 1984; *Paterson and Luan*, 1990; *Rutter and Brodie*, 2004b, see Table 4). For
754 some earlier data acquired with solid-medium apparatus, a large uncertainty is
755 attributed to imprecise stress measurements in the solid-medium deformation
756 apparatus (e.g., *Gleason and Tullis*, 1995). However, a large part of the lack of
757 precision and accuracy of the solid medium apparatus is caused by friction and errors
758 associated with the hit point determination. Strain-rate-stepping experiments should
759 not be affected by this error, because all data within a single experiment is determined
760 with respect to the same hit point, and only a slope is fitted to the data, regardless of
761 the absolute values of stresses. In addition, a recent study indicates good accuracy for
762 stresses derived from Griggs apparatus (*Richter et al.*, 2016). Furthermore, the lack of
763 evidence for partial melting in our samples would be consistent with expected low
764 values for stress exponents as suggested by *Jaoul et al*., (1984); *Luan and Paterson*
765 (1992).

766 Stress exponents can only be correlated with deformation processes if steady
767 state conditions are reached. Achieving this state may be especially problematic for
768 regime 1 conditions (*Hirth and Tullis*, 1994). The required high strain conditions are
769 difficult to achieve in coaxial compression experiments. Our shear experiments are
770 deformed to high shear strain (up to $\gamma \sim 5$) where mechanical and microstructural
771 steady state is more or less achieved, at least at high temperatures (800-1000 °C; Fig.
772 2). Hence, the low stress exponents cannot be explained by incomplete steady state
773 conditions as suggested by *Gleason and Tullis* (1995). In addition, *Gleason and Tullis*
774 (1995) associate low stress exponents with the transition from regime 2 to regime 1
775 after *Hirth and Tullis* (1992). Such a temperature dependent microstructural change is

776 not observed in our samples used for calculating stress exponents. However, the
777 observed microstructures indicate dislocation creep and diffusion creep between 800
778 °C and 1000 °C. In contrast, dislocation creep was solely inferred in earlier studies
779 (e.g., *Gleason and Tullis*, 1995; *Jaoul et al.*, 1984). These studies used quartzites with
780 narrow grain-size ranges and large average grain sizes where grain-size-sensitive
781 deformation mechanisms are unlikely. The broad grain-size range of our starting
782 material with a pronounced fine-grained fraction enables grain-size-sensitive diffusion
783 creep in addition to grain-size-insensitive dislocation creep resulting in mixed stress
784 exponents.
785
786 5.7 Extrapolation to natural conditions
787 It is important to attempt the extrapolation of experimental results to natural
788 conditions. As a first step, the different mechanical and microstructural criteria should
789 be combined to delineate the BVT. In the present study, sample deformation was
790 classified as viscous, semi-brittle, and transitional on the basis of the microstructural
791 suites and experimental behaviour, where transitional deformation is defined by the
792 presence of many remaining large clasts coexisting with clusters of recrystallised
793 grains, the fabric dominated by shear bands at high shear strain. Deformation
794 microstructures can be plotted for the same strain rate in a differential stress vs.
795 confining pressure diagram at a strain rate of $2.5 \cdot 10^{-5}$ s^{-1} (Fig. 14a). The transitional
796 samples all plot above the Goetze criterion, so that the Goetze criterion, as to be
797 expected, marks the upper stress limit of dominantly viscous deformation
798 mechanisms. For high confining pressures (1.5 GPa), the BVT can be well delineated
799 using the microstructures and strain rate - temperature relationships (Fig. 14b),
800 although the Goetze criterion is more difficult to define at low temperatures. Using the

broad division boundary (green line) from the experimental data, the BVT can be extrapolated to natural conditions of strain rate and temperature (Fig. 14c). As can be seen, the extrapolation is in fairly good agreement with the well documented BVT data point of *Stipp et al.* (2002a,b) for a strain rate of ~10^{-12} s^{-1}. For the representative natural conditions (280 °C, P_c = 300 MPa, $\Delta\sigma$ = 250 MPa), the stresses, which were determined were converted to strain rates using the flow law from *Hirth et al.* (2001) and recalculated for 1.5 GPa confining pressure using the appropriate water fugacity values. The microstructures of the *Stipp et al.* (2002a,b) sample at 280 °C are within the viscous field at stresses just below the brittle conditions, consistent with the Goetze criterion and the extrapolation from this study. If natural conditions of 1.0 GPa confining pressures are used, our corrected results for P_c = 1 GPa and the *Stipp et al.* (2002a,b) data are consistent, too (Fig. 14d). For 0.5 GPa confining pressure, our experiments have only one data point, but it is also consistent with the extrapolation derived from the series of experiments at higher pressure (Fig. 14d). Thus, this extrapolation should serve as a guideline to determine the BVT in quartz for a wide range of conditions between experiments and nature. For example, semibrittle microstructures in rocks at elevated temperatures in quartz could be used to infer minimum strain rates.

Insert Figure 14 here

If creep conditions of laboratory data for quartz are to be extrapolated to natural conditions, a power-law behaviour (Eq. 1) is always assumed. Existing and commonly used flow laws assume pure dislocation creep with a relatively high stress exponent, typically n = 4 (*Hirth et al.*, 2001; *Paterson and Luan*, 1990). Our flow law parameter of a stress exponent of n = 1.9 (Table 4) introduces combined (mixed mode) deformation mechanisms of dislocation and diffusion creep. It should be

826 pointed out that the stress exponent for silica gel in the experiments by *Luan and*
827 *Paterson* (1992) also show a value of n = 2.3, the data by *Jaoul et al.*, (1984) show n
828 = 1.4 to 2.4, and *Kronenberg and Tullis* (1984) show n = 2.5 for novaculite. Thus,
829 several studies have determined stress exponents of n ≈ 2, independently from each
830 other. The reason why these stress exponents have been questioned in the past is that
831 either impurities (*Luan and Paterson*, 1992) or melt (*Jaoul et al.*, 1984) may have
832 affected the rheology of the samples. In our case, no melt was detected, and we can
833 demonstrate the effect of smaller and larger grain-size fractions for the activation of
834 different deformation mechanisms. Our value for the activation energy is greater than
835 those of *Hirth et al.* (2001) and *Kronenberg and Tullis* (1984) and less than those of
836 *Rutter and Brodie* (2004) and *Gleason and Tullis* (1995), but the range of values is
837 consistent with previous determinations (Table 4).

838 When our data are extrapolated to low temperatures at natural strain rates, the
839 BVT in terms of temperature, strain rate, and pressure will very much depend on the
840 grain size, where small sizes that are very common at low temperatures will favour the
841 operation of diffusion creep mechanism, which are part of the inferred deformation
842 mechanisms in this study. In nature, the expected deformation process probably is
843 solution precipitation creep. It is an important result of this study that the BVT in
844 quartz is not simply a transition from cracking to crystal-plastic deformation, but,
845 instead, it involves grain-size dependent diffusion-creep processes, too.

846 Cataclasis is a very efficient process to reduce grain size, so that our simulated
847 cataclasite is an appropriate starting material for studying the deformation history
848 dependent transition from cracking to viscous deformation. The results clearly show
849 that cataclasites are very likely candidates for subsequent viscous deformation. This
850 interplay of brittle and viscous deformation processes is particularly applicable to high

851 stress deformation settings such as seismically active deformation zones. Catclasis
852 will provide the fine-grained material, which helps to accommodate aseismic creep in
853 interseismic periods, i.e., postseismic creep deformation.
854
855 6. Conclusions
856 A set of shear experiments performed on quartz material under elevated
857 confining pressures (predominantly 1.5 GPa) and temperatures (500 °C - 1000 °C) at
858 intermediate to fast shear strain rates ($3.5 \cdot 10^{-6}$ s^{-1} to ~$2 \cdot 10^{-3}$ s^{-1}) documents the
859 transition from (semi)-brittle to viscous deformation. The Goetze criterion ($\Delta\sigma > P_c$) is
860 confirmed to delineate the upper limit of differential stress for viscous deformation.
861 Samples above the Goetze criterion are characterised by Riedel fractures or
862 shear bands at high shear strain, normal geological friction coefficients, and *n*-values
863 too high for dislocation creep. At low temperatures, increasing confining pressure
864 causes increasing strength, as is to be expected for fracturing and frictional
865 deformation. A somewhat unsystematic temperature-dependence of stress is observed
866 under these conditions. Cataclastic flow partly accompanied by stress-induced
867 dissolution precipitation is suggested as the dominating deformation process at
868 temperatures just below the transition to viscous deformation (650°C) for a strain rate
869 of 2.5 x 10^{-5} s^{-1}, indicated by a power-law breakdown with a stress exponent of n = 6.4
870 ± 1.3.
871 Below the Goetze criterion ($\Delta\sigma < P_c$), viscous deformation dominates, as
872 demonstrated by weakening of samples with increasing pressure and temperature. The
873 microstructure is dominated by a pervasive foliation at high shear strain accompanied
874 by an increasing recrystallised grain size with increasing temperature, only partially
875 dependent on flow stress. Presence of different CPO´s in different grain-size fractions

and the stress exponents ($n = 1.9 \pm 0.6$) indicate a combination of diffusion creep and dislocation creep. It is argued that diffusive mass transfer and grain-boundary-sliding prefer the small grain-size fraction while dislocation creep is more effective in large grains. The constant stress exponent between 800 °C and 1000 °C suggests no change in the rate-limiting factor and a similar activation energy for the diffusion and dislocation creep mechanism.

From these results, it can be inferred that the brittle to viscous transition with increasing temperature in nature may occur as a combination of diffusion and dislocation creep. The combination favours the viscous deformation to occur in fine grained aggregates likely to have formed by previous cataclastic deformation. Such a sequential transition in time elegantly explains the alternation of episodic seismic (brittle) and aseismic deformation in high stress, seismically active zones.

Acknowledgments

We would like to thank Rüdiger Kilian for extensive stimulating discussions and help with the MTEX toolbox. Furthermore, we wish to thank Willy Tschudin for preparing excellent thin sections, Hans-Rudolf Rüegg for supplying equipment in the deformation lab, Trine Merete Dahl for preparing thin sections for EBSD, and the team of the Nano Imaging Lab and Tom Ivar Eilertsen for support with the SEM. Raw data and samples can be acquired at the corresponding author. Constructive and insightful reviews of 2 anonymous reviewers and Raphael Gottardi and he very constructive input by the editor William Dunne have substantially improved the manuscript. Funding by the Swiss National Science Foundation grant no. 200021-138216 is thankfully acknowledged.

901 References

902 Barber, D. J., Wenk, H.-R., Hirth, G., Kohlstedt, D. L. (2010) Dislocations in
903 minerals In: Hirth, J. P., Kubin, L. (Ed.) Dislocation in solids, Elsevier, 171-232,
904 doi:10.1016/SI572-4859(09)01604-0

905 Bell, R. L., Langdon, T. G. (1967) An investigation of grain-boundary sliding
906 during creep, Journal of Material Science, 2, 313-323

907 Berthé, D, Choukroune, P., Jegouzo, P. (1979) Orthogneiss, mylonite and non
908 coaxial deformation of granites: the example of the South Armorican Shear Zone,
909 Journal of Structural Geology, 1, 31-42

910 Blanpied, M. L., Lockner, D. A., Byerlee, J. D., (1995) Frictional slip of
911 granite at hydrothermal conditions, Journal of Geophysical Research, 100, 13045-
912 13064

913 Brace, W. F., Kohlstedt, D. L. (1980) Limits on lithospheric stress imposed by
914 laboratory experiments, Journal of Geophysical Research: Solid Earth, 85, 6248-6252

915 Byerlee, J. D. (1968) Brittle-ductile transition in rocks, Journal of Geophysical
916 Research, 73, 4741-4750

917 Byerlee, J. (1978) Friction of Rocks, Pure and Applied Geophysics,116, 615-
918 626, doi:10.1007/BF00876528

919 Chester, F M., Higgs, N. G. (1992) Multimechanism friction constitutive
920 model for ultrafine quartz gouge at hypocentral conditions, Journal of Geophysical
921 Research, 97, 1859-1870

922 Cross, A. J., Priop, D. J., Stipp, M., Kidder, S. (2017) The recrystalliued grain
923 size piezometer for quartz: An EBSD-based calibration, Geophysical Research
924 Letters, 44, 6667-6674, doi:10.1002/2017GL073836

925 Edington, J. W., Melton, K. N., Cutler, C. P. (1976) Superplasticity, Progress
926 in Material Science, 21, 61-158
927 FitzGerald, J. D., Boland, J. N., McLaren, A. C., Ord, A., Hobbs, B. E. (1991)
928 Microstructures in water-weakened single crystals of quartz, Journal of Geophysical
929 Research, 96, 2139-2155
930 Farver, J., and Yund, R. (2000) Silicon diffusion in a natural quartz aggregate:
931 constraints on solution-transfer diffusion creep, Tectonophysics, 325, 193-205
932 Giletti, B. J., and Yund, R. A. (1984) Oxygen diffusion in quartz, Journal of
933 Geophysical Research, 89, 4039-4046
934 Gleason, G. C., and Tullis, J. (1995) A flow law for dislocation creep of quartz
935 aggregates determined with the molten salt cell, Tectonophysics, 247, 1-23
936 Gomez Barreiro, J., Lonardelli, I., Wenk, H. R., Dresen, G., Rybacki, E.,
937 Tomé, C. N. (2007) Preferred orientation of anorthite deformed experimentally in
938 Newtonian creep, Earth and Planetary Science Letters, 264, 188-207
939 Handy, M. R. (1989) Deformation regimes and the rheological evolution of
940 fault zones in the lithosphere: the effects of pressure, temperature, grainsize and time,
941 Tectonophysics, 163, 119-152
942 Hansen, L. N., Zimmerman, M. E., Kohlstedt, D. L. (2011) Grain boundary
943 sliding in San Carlos olivine: Flow law parameters and crystallographic-preferred
944 orientation, Journal of Geophysical Research, 116, B08201,
945 doi:10.1029/2011JB008220
946 Heilbronner, R., and Barrett, S. (2014) Image analysis in earth sciences,
947 Springer Berlin Heidelberg, p. 520

948 Heilbronner, R., and Kilian, R. (2017) The grain size(s) of Black Hills
949 Quartzite deformed in the dislocation creep regime, Solid Earth,
950 https://doi.org/10.5194/se-8-1071-2017
951 Heilbronner, R., and Tullis, J. (2002) The effect of static annealing on
952 microstructures and crystallographic preferred orientations of quartzites
953 experimentally deformed in axial compression and shear, Geological Society, London,
954 Special Publications, 200, 191-218, doi:10.1144/GSL.SP.2001.200.01.12
955 Heilbronner, R., and Tullis, J. (2006) Evolution of c axis pole figures and grain
956 size during dynamic recrystallization: Results from experimentally sheared quartzite,
957 Journal of Geophysical Research, 111, B10202, doi:10.1029/2005JB004194
958 Hielscher, R., and Schaeben, H. (2008) A novel pole figure inversion method:
959 specification of the MTEX algorithm, Journal of Applied Crystallography, 41, 1024-
960 1037, doi:10.1107/S0021889808030112
961 Hirth, G., Teyssier, C., Dunlap, W. J. (2001) An evaluation of quartzite flow
962 laws based on comparisons between experimentally and naturally deformed rocks,
963 International Journal of Earth Science, 90, 77-87, doi:10.1007/s005310000152
964 Hirth, G., and Tullis, J. (1992), Dislocation creep regimes in quartz aggregates,
965 Journal of Structural Geology, 14, 145-159, doi:10.1016/0191-8141(92)90053-Y
966 Hirth, G., and Tullis, J. (1994), The brittle-plastic transition in experimentally
967 deformed quartz aggregates, Journal of Geophysical Research, 99, 11731-11747,
968 doi:10.1029/93JB02873
969 Jaoul, O., Tullis, J., Kronenberg, A. (1984) The effect of varying water
970 contents on the creep behaviour of Heavitree quartzite, Journal of Geophysical
971 Research, 89, 4298-4312

Karato, S., Jung, H., Katayama, I., Skemer, P. (2008) Geodynamic significance of seismic anisotropy of the upper mantle: new insights from laboratory studies, Annu. Rev. Earth Planet. Science, 36, 59-95, doi:10.1146/annurev.earth.36.031207.124120

Keulen, N., Stünitz, H., Heilbronner, R. (2008): Healing microstructures of experimental and natural fault gouge. – J. Geophys. Research, doi:10.1029/2007JB005039

Kilian, R., and Heilbronner, R. (2017) Texture analysis of experimentally deformed Black Hills Quartzite, Solid Earth, https://doi.org/10.5194/se-8-1095-2017

Kohlstedt, D. L., Evans, B., Mackwell, S. J. (1995) Strength of the lithosphere: Constraints imposed by laboratory experiments, Journal of Geophysical Research, 100, 17,587-17,602, doi:10.1029/95JB01460

Kohlstedt, D. L., and Hansen, L. N., (2015) Constitutive equations, rheological behaviour, and viscosity of rocks, In: Schubert, G. (Ed.) Treatise on geophysics, 2nd edition, Vol. 2, Oxford: Elsevier, 441-472

Kronenberg, A. K., and Tullis, J. (1984) Flow Strengths of Quartz Aggregates: Grain Size and Pressure Effects due to Hydrolytic Weakening. Journal of Geophysical Research, 89, 4281-4297, doi:10.1029/JB089iB06p04281

Luan, F. C.,and Paterson, M. S. (1992) Preparation and deformation of synthetic aggregates of quartz, Journal of Geophysical Research, 97, 301-320

Menegon, L., Pennachioni, G., Heilbronner, R., Pittarello, L. (2008) Evolution of quartz microstructure and *c*-axis crystallographic preferred orientation within ductilely deformed granitoids (Arolla unit, Western Alps), Journal of Structural Geology, 30, 1332-1347, doi:10.1016/j.jsg2008.07.007

996 Orowan, E. (1940) Problems of plastic gliding, Proceedings of the Physical
997 Society, 52, 8-22
998 Panozzo, R., and Hürlimann, H. (1983) A simple method for the
999 discrimination of convex and convex-concave lines, Microscopica Acta, 87, 169-176
1000 Paterson, M. S. (1989) The interaction of water with quartz and its influence in
1001 dislocation flow – an overview, In: Karato, S.-I., and Toriumi, M. (Ed.), Rheology of
1002 solids and of the earth, Oxford Univiversity Press, Oxford, 107-142
1003 Paterson, M. S. (2013) Materials science for structural geology, Springer
1004 Dordrecht Heidelberg New York London, p. 247, doi:10.1007/978-94-007-5545-1
1005 Paterson, M. S., and Luan, F. C. (1990) Quartzite rheology under geological
1006 conditions, In: Knipe, R. J., Rutter, E. H. (eds.), Deformation mechanisms, rheology
1007 and tectonics, Geological Society Special Publication, 54, 299-307
1008 Paterson, M. S., and Wong, T. (2005) Experimental rock deformation - the
1009 brittle field, Springer Berlin Heidelberg, p. 347, doi:10.1007/b137431
1010 Pec, M., Stünitz, H., Heilbronner, R. (2012) Semi-brittle deformation of
1011 granitoid gouges in shear experiments at elevated pressures and temperatures, Journal
1012 of Structural Geology, 33, 200-221, doi:10.1016/j.jsg.2011.09.001
1013 Pec, M. (2014), Experimental investigation on the rheology of fault rocks,
1014 dissertation, Basel Universität, Basel
1015 Poirier, J.P., and Guillope, M. (1979) Deformation induced recrystallization of
1016 minerals, Bull. De. Mineral. 102, 67-74.
1017 Précigout, J., Stünitz, H. (2016): Evidence of phase nucleation during olivine
1018 diffusion creep: A new perspective for mantle strain localization. - Earth and
1019 Planetary Science Letters, 455, p. 94-115, doi.org/10.1016/j.epsl.2016.09.029

1020 Richter, B, Stünitz, H., Heilbronner, R. (2016) Stresses and pressures at the
1021 quartz-to-coesite transformation in shear deformation experiments, Journal of
1022 Geophysical Research: Solid Earth, 121, doi:10.1002/2016JB013084
1023 Rutter, E. H., and Brodie, K. H. (2004a) Experimental grain size-sensitive flow
1024 of hot pressed Brazilian quartz aggregates, Journal of Structural Geology, 26:11,
1025 2011-2023
1026 Rutter, E. H., and Brodie, K. H. (2004b) Experimental intracrystalline plastic
1027 flow in hot pressed synthetic quartzite prepared from Brazilian quartz crystals, Journal
1028 of Structural Geology, 26, 259-270, doi: 10.1016/S0191-8141(03)00096-8
1029 Schmid, S. M., and Casey, M. (1986) Complete fabric analysis of some
1030 commonly observed quartz c-axis patterns, Geophysical Monographs, 36, 263-286
1031 Schmid, S. M., Panozzo, R., Bauer, S. (1987) Simple shear experiments on
1032 calcite rocks: rheology and microfabric, Journal of Structural Geology, 9, 747-778
1033 Scholz, C. H. (2007) The Mechanics of Earthquakes and Faulting, 2nd edition,
1034 Cambridge University Press, Cambridge, p. 471
1035 Sibson, R. H. (1989) Earthquake faulting as a structural process, Journal of
1036 Structural Geology, 11, 1-14, doi:10.1016/0191-8141(89)90032-1
1037 Stipp, M., Stünitz, H., Heilbronner, R., Schmid, S. M. (2002a) Dynamic
1038 recrystallisation of quartz: correlation between natural and experimental conditions,
1039 Geological Society, London, Special Publications, 200, 171-190,
1040 doi:10.1144/GSL.SP.2001.200.01.11
1041 Stipp, M., Stünitz, H., Heilbronner, R. & Schmid, S. M. (2002b):
1042 DynamicRecrystallization of quartz: Correlation between Natural and Experimental
1043 Conditions. In: S. de Meer, M. R. Drury, J. H. P. de Bresser & G. M. Pennock:
1044 Deformation Mechanisms, Rheology and Tectonics: Current Status and Future

1045 Perspectives. - Geological Society, London, Special Publications 200, 171-190.

1046 Stünitz, H., Thust, A., Behrens, H., Kilian, R., Tarantola, A., FitzGerald, J. D.
1047 (2017) Water redistribution in experimentally deformed natural milky quartz single
1048 crystals – Implications for H_2O-weakening processes, Journal of Geophysical
1049 Research: Solid Earth, 122, doi:10.1002/2016JB013533

1050 Tarantola, A., Diamond, L. W., Stünitz, H. (2010) Modification of fluid
1051 inclusions in quartz by deviatoric stress I: experimentally induced changes in
1052 inclusion shapes and microstructures, Contribution to mineralogy and Petrology, 160,
1053 825-843, doi:10.1007/s00410-101-0509-z

1054 Tarantola, A., Diamond, L. W., Stünitz, H., Thust, A., Pec, M. (2012)
1055 Modification of fluid inclusion in quartz ba deviatoric stress III: Influence of principal
1056 stresses on inclusion density and orientation, Contribution to Mineralogy and
1057 Petrology, 164, 537-550, doi:10.1007/s00410-012-0749-1

1058 Trepmann C. A., and Stöckhert B. (2003) Quartz microstructures developed
1059 during non-steady state plastic flow at rapidly decaying stress and strain rate, Journal
1060 of Structural Geology, 25. 2035-2051, doi:10.1016/S0191-8141(03)00073-7

1061 Trepmann, C. A., Stöckhert, B. (2013) Short-wavelength undulatory extinction
1062 in quartz recording coseismic deformation in the middle crust – an experimental
1063 study, Solid Earth, 4, 263-276, doi:10.5194/se-4-263-2013

1064 Tullis, J. (2002) Deformation of granictic rocks: Experimental studies and
1065 natural examples In: Karato, S.I. and Wenk, H.-R., Plastic deformation of minerals
1066 and rocks, Reviews in mineralogy and Geochemistry, 51, 51-95,
1067 doi:10.2138/gsrmg.51.1.51

Tullis, J., Shelton, G. L., Yund, R. A. (1979) Pressure dependence of rock strength: implications for hydrolytic weakening, Bulletin de Minéralogie, 102, 110-114

Tullis, J., and Yund, R.A. (1977) Experimental deformation of dry Westerly granite, Journal of Geophysical Research, 82, 5705–5718

Twiss, R. J., and Moores, E. M. (2007) Structural geology, W. H. Freeman and Company, New York, Second Edition, p. 736

Van Daalen, M., Heilbronner, R., Kunze, K. (1999) Orientation analysis of localized shear deformation in quartz fibres at the brittle–ductile transition, Tectonophysics, 303, 83-107

Yund, R.A., and Tullis, J. (1991) Compositional changes of minerals associated with dynamic recrystallisation, Contributions to Mineralogy and Petrology, 108, 346–355

Figures and tables

Figure 1: Sample assembly.

(a) Sample (quartz powder) is inserted between 45° pre-cut forcing blocks, in a jacket surrounded by confining medium (NaCl) and a carbon furnace (after *Richter et al.*, 2016). Displacement in the shear zone is at 45° to the plane of drawing. (b) Stresses in the sample: F = load applied to upper forcing block, P_c = confining pressure, σ_n = normal stress, τ = shear stress.

Figure 2: Stress-strain curves for constant shear strain rate experiments. Confining pressure is 1.5 GPa; horizontal lines mark the Goetze criterion. (a)

1093 Shear experiments at different temperatures; arrow indicates assumed initiation of slip
1094 at sample - forcing block interface. (b) Experiments with different shear strain rates at
1095 650 °C, 800 °C and 900 °C. (c) Experiments with different starting material: crushed
1096 = gouge ($d \leq 100$ µm); hot pr. = gouge ($d \leq 100$ µm), hot pressed before deformation
1097 (20h at 1000°C, 1.5 GPa); sieved = gouge ($7 \leq d \leq 11$ µm); arrow indicates the onset
1098 of forcing block deformation.
1099
1100 Figure 3: Stress-strain curves to demonstrate the influence of confining
1101 pressure at three different temperatures.
1102 Strain rate is $2.5 \cdot 10^{-5}$ s^{-1}; horizontal lines mark the Goetze criterion for
1103 different confining pressures.
1104
1105 Figure 4: Stress-strain curves for strain rate stepping experiments.
1106 Stress-strain curves for experiments at 650 °C, 800 °C, 900 °C, 1000 °C and
1107 800 °C (hot pressed; dashed line as in Fig. 2) are shown in comparison with constant
1108 shear strain rate experiments (numbers 500br, 499br, 412br, 388br, 337br, 419br) at
1109 same conditions. Confining pressure is 1.5 GPa in all samples; horizontal lines mark
1110 the Goetze criterion. The arrow at 488br (800 °C) points to a failure of the experiment.
1111 The arrow at 482br (900 °C) at very high strain marks the change of sample geometry
1112 due to collision of forcing blocks.
1113
1114 Figure 5: Starting material.
1115 Quartz powder after run-in of the σ_1 piston but before the hit point (pre-
1116 deformation) at 800 °C and 1000 °C. (a) Light micrograph of sample 487br at
1117 T=800°C and Pc=1.5 GPa, total time of experiment: 25h. Look-up table in upper right

indicates circular polarisation. (b) SEM/band contrast image of sample 487br. (c) Light micrograph of sample 417br at T=1000°C and Pc=1.5 GPa, total time of experiment: 20h. Look-up table in upper right indicates crossed polarisation. (d) SEM/band contrast image of sample 417br. SEM and light micrographs do not show the same regions.

Figure 6: Microstructures across the brittle-to-viscous transition.

High strain samples deformed at temperatures between 500 °C and 1000°C, 1.5 GPa and ~10^{-5} s^{-1}. Look-up tables indicate circular polarisation for all micrographs, except 450br and 435br which are cross polarised; sinistral shear sense applies to all. Left two columns: experiments using crushed starting material, right column: experiments with hot pressed starting material. Solid lines (F) indicate orientation of foliation; dashed lines indicate shear band orientation (SB); dotted lines mark Riedel surfaces (R and R'), schematic of Riedel geometry in inset lower right.

Figure 7: Dependence of microstructures on confining pressure and strain rate.

Look-up tables indicate circular polarisation or crossed polarisation; sinistral shear sense applies to all. Solid lines (F) indicate orientation of foliation; dashed lines indicate shear band orientation (SB); dotted lines mark Riedel surfaces (R).

Figure 8: Brittle structures at high temperature.

Sample (386br) deformed at 800 °C , 0.5 GPa and ~10^{-5} s^{-1}. (a) Light micrograph showing fracturing; look-up tables indicate crossed polarisation; dotted lines mark Riedel surfaces (R and R'). (b) SEM/BSE micrograph of very fine-grained material generated by comminution along Riedel fractures.

1143

1144 Figure 9: Grain size distribution of recrystallised grains.

1145 Histograms show volume weighted frequency distributions of the diameter of
1146 volume equivalent spheres (D_{equ}); modal values are indicated. Grain size maps for
1147 samples deformed between 700°C and 1000°C are shown with the same magnification
1148 (see scale) and color coded such that blue to yellow corresponds to $2\mu m \leq D \leq 9\mu m$.
1149 (a) Grain size distributions for standard starting material ($d \leq 100$ µm). (b) Special
1150 starting material for comparison: hot pr. = hot pressed before deformation; sieved =
1151 starting material ($7 \leq d \leq 11$ µm).

1152

1153 Figure 10: Internal misorientation density of recrystallised grains.

1154 Two measures for misorientation density at the grain scale are evaluated for
1155 samples deformed at temperatures from 700 °C to 1000 °C; gKAM = grain kernel
1156 average misorientation (*Heilbronner and Kilian*, 2017); GOS_{la} = grain orientation
1157 spread, normalised for long axis (see text); for each data point, the PARIS factor is
1158 colour coded and the symbol size is related to the equivalent diameter.

1159

1160 Figure 11: Textures for different grain size fractions.

1161 Textures are shown for samples with standard starting material (crushed),
1162 deformed at 700 °C to 1000 °C, standard confining pressure of 1.5 GPa, and standard
1163 strain rate of $2.5 \cdot 10^{-5}$ s^{-1}. For each temperature, [*c*], [*a*], and [*r*] pole figures are shown
1164 for all recrystallised grains in the range of ($d \leq 25$ µm) (top row), for the small grain
1165 size fraction (middle row) and the large grain size fraction (bottom row); the
1166 delimiting grain size is indicated. Contouring interval = 1 m.u.d.; pole figure
1167 maximum in the upper left and pole figure J-index on the lower right of the pole

figure.

Figure 12: Friction coefficients for different experimental conditions.

Friction coefficient is calculated from shear and normal stress on sample: $\mu = \tau / \sigma_n$ (Figure 1). (a) Different shear strain rates at constant confining pressure of 1.5 GPa. (b) Different confining pressures at constant shear strain rate of $2.5 \cdot 10^{-5}$ s^{-1}.

Figure 13: Derivation of stress exponent and activation energy.

(a) At 650 °C, the stress exponent n ~ 6.4. For 800 °C -1000 °C, the average of the stress exponent is determined: n = 1.9±0.6. (b) From experiments at strain rates of 10^{-4} s^{-1} and 10^{-5} s^{-1}, the activation energy is derived: Q ~ 170 kJ/mol. (II) indicates the second measurement of stress at a given strain rate in strain rate stepping experiments (cf. Table 2). (c) At 800°C, 1.5 GPa and 10^{-5} s^{-1}, and for a stress exponent n = 1.9, the grain size exponent p is 1.08; m = slope of liner fit. Samples used: 388br = standard starting material; 419br = hot pressed at 1000°C; 445br = sieved to ($7 \leq d \leq$-11µm).

Figure 14: Extrapolation of the brittle-to-viscous transition from the lab to nature.

Discrimination of 'brittle', 'transitional' and 'viscous' is based on microstructure. (a) Differential stress versus confining pressure for experimental samples and one natural samples. (b) Shear strain rate versus temperature for experimental samples deformed at constant confining pressure; black numbers = flow stress; grey numbers = peak stress; green line traces the brittle-to-viscous transition (BVT). (c) Extrapolation of (b) to natural conditions. The transition of a natural sample (*Stipp et al.* (2002)) is indicated; water fugacity is considered after *Hirth et al.*,

1193 (2001). (d) Same extrapolation as in (c) using additional data points recalculated for
1194 1.0 GPa (orange) and 0.5 GPa (blue) confining pressure; filled circles - using flow
1195 law after *Hirth et al.*, 2001; open circles - using flow law of this study.
1196
1197
1198 Table 1: Experimental conditions for constant shear strain rate experiments.
1199 1) Pre-treatment: Hot pressed = 20 hours at 1000°C and 1.5-1.6 GPa. Sieved = powder
1200 sieved to grain size fraction ($7 \leq d \leq 11$ µm).
1201 2) Friction coefficient determined at peak stress.
1202
1203 Table 2: Experimental conditions for shear strain rate stepping experiments.
1204 1) Temperature approximate due to technical problem with furnace.
1205 2) Approximate value due to power failure.
1206 3) Sample hot pressed for 20 hours at 1000°C and 1.5-1.6 GPa.
1207 4) Hardening at end of experiment due to contact of forcing blocks.
1208
1209 Table 3: Grain size analysis
1210 1) Arithmetic mean of area equivalent diameters of circles (d_{equ})
1211 2) Median of d_{equ}
1212 3) Root-mean-square of d_{equ}
1213 4) Mode = Mean of Gaussian curve fit to volume weighted histogram of volume
1214 equivalent diameters of spheres (D_{equ})
1215 5) Standard deviation of Gaussian curve fit.
1216 6) Hot pressed (24 h) undeformed sample
1217 7) Hot pressed (20 h) undeformed sample

1218 8) Hot pressed (20 h) at 1000°C and 1.5-1.6 GPa.

1219 9) Powder sieved to grain size fraction ($7 \leq d \leq 11$ µm).

1220

1221 Table 4: Selection of flow law parameters from literature.

1222

Sample	Temperature (°C)	Confining Pressure (MPa)	Pre-treatment[1)]	Shear strain	Shear strain rate (s^{-1})	Maximum differential stress (MPa)	Friction coefficient ($\mu = \tau / \sigma_n$) at $\gamma = 3$	Microstructure (for $\gamma > 3$)
340br[2)]	500	1510		1.6	1.4	2738	0.47	-
450br	500	1540		3.2	2.1	3212	0.46	brittle
338br[2)]	600	1522		1.4	1.4	2513	0.45	-
479br	600	1538		3.9	2.1	2423	0.43	brittle
415br	600	1512	hot pressed	3.0	1.9	3246	0.51	brittle
435br	650	1507		3.6	2.1	2698	0.46	transitional
481br	650	1554		4.2	3.0	2538	0.43	transitional
380br	700	1500		0.0	0.0	0	0.00	-
339br[2)]	700	1524		2.0	2.1	1298	0.30	-
437br[2)]	700	1529		1.7	1.9	1483	0.32	-
383br	700	1585		4.9	2.8	1246	0.25	viscous
493br	700	1512	hot pressed	4.9	2.7	2051	0.39	transitional
487br	800	1511		0.0	0.0	0	0.00	-
439br[2)]	800	1526		1.4	2.1	856	0.22	-
388br	800	1527		4.8	2.8	858	0.21	viscous
445br	800	1578	sieved	4.7	3.0	415	0.09	viscous
419br	800	1556	hot pressed	4.2	2.8	1159	0.25	viscous
412br	900	1530		2.9	2.8	475	0.10	viscous
417br	1000	1576		0.0	0.0	0	0.00	-
337br	1000	1506		3.2	3.0	152	0.05	viscous
494br	650	1088		5.7	4.8	2396	0.49	transitional
452br	700	1064		4.4	2.7	1536	0.40	transitional
448br	800	1067		4.5	2.9	864	0.25	viscous
386br	800	574		3.2	2.3	1500	0.53	brittle
500br	650	1502		1.1	0.3	1276	0.30	-
447br	800	1556		4.1	27.0	1783	0.35	transitional
499br	900	1535		4.0	189.0	2015	0.39	transitional

Sample	Temperature (°C)	Confining Pressure (MPa)	Shear strain	Stress exponent	Shear strain rate (s^{-1})	Flow stress (MPa)	Friction coefficient ($\mu = \tau / \sigma_n$)
498br	650[1)]	1589	5.4	6.4	2.60	2608	0.46
					1.20	2517	0.44
					0.30	1842	0.36
488br	800	1623	6.4	1.8	28.00	1811	0.37
					5.10	783	0.20
					1.20	422	0.11
					0.48[2)]	250	0.07
480br[3)]	800	1601	4.5		2.30	1040	0.25
					0.63	293	0.09
					2.70	820	0.20
482br	900	1583	8.4	2.0	28.00	1272	0.29
					3.60	389	0.11
					0.49	178	0.05
					41.00[4)]	1494	0.32
485br	1000	1588	6.2	1.8	27.00	578	0.16
					4.00	189	0.06
					0.37	75	0.02
					34.00	794	0.20

Sample	T [°C]	Pc [GPa]	$\dot{\gamma}$ [$10^{-5}\cdot s^{-1}$]	Width [px]	Height [px]	Step size [µm]	No. of grains	2D mean[1)] [µm]	2D median[2)] [µm]	2D RMS[3)] [µm]	3D mode[4)] [µm]	3D st.dev.[5)] [µm]
487br[6)]	800°	1.5	-	700	625	0.20	386	5.21	4.31	6.50	9.1	2.7
417br[7)]	1000°	1.5	-	1250	1649	0.20	583	7.56	6.65	9.21	12.8	4.3
383br	700	1.5	2.8	525	325	0.20	3988	0.98	0.75	1.41	2.1	0.5
388br	800	1.5	2.8	500	500	0.20	1517	2.27	1.86	2.90	4.1	1.9
412br	900	1.5	2.8	925	850	0.20	2789	3.02	2.67	3.79	6.1	0.9
337br	1000	1.5	3	1250	1000	0.20	696	5.80	4.53	7.99	15.3	13.4
493br[8)]	700	1.5	2.7	400	350	0.20	3518	0.93	0.77	1.36	1.6	0.2
419br[8)]	800	1.5	2.8	800	900	0.15	2257	2.34	1.99	3.00	4.8	0.8
445br[9)]	800	1.5	3	1200	700	0.10	2495	1.30	0.78	2.05	4.4	3.7
452br	700	1	2.7	820	600	0.15	9716	0.77	0.63	1.12	1.5	0.2
448br	800	1	2.9	1600	900	0.10	4102	1.49	1.17	2.1	3.3	0.5
447br	800	1.5	27	1000	750	0.20	16390	1.173	1.01	1.51	2.0	0.3
499br	900	1.5	189	708	512	0.20	11521	0.914	0.81	1.22	1.5	0.2

Source	Confining pressure Pc [GPa]	Stress exponent n	Activation energy Q [kJ/mol]	Factor A [MPa-1 s-1]	Material	Water content
Jaoul et al. (1984)	1.5	1.4 – 2.4	146 - 172	$2.95 \cdot 10^{-4}$ to $7.68 \cdot 10^{-8}$	Heavitree Quartzite d = 0.2 mm	H_2O in different amounts
Kronenberg & Tullis (1984)	0.9 – 1.45	2.9 – 3.2	170 - 220	-	Heavitree Quartzite d = 211 µm	As-is
Kronenberg & Tullis (1984)	1.5	2.5	120 - 150	-	Novaculite d = 4.9 µm	0.4 wt% H_2O added
Paterson & Luan (1990)	0.3	2.3	150	-	Silica Gel d = 30 – 80 µm	1000 – 10000 H/106 Si
Paterson & Luan (1990)	0.3	3.9	150	$\sim 4.0 \cdot 10^{-10}$	Silicic Acid d = 20 µm	1000 – 10000 H/106 Si
Gleason & Tullis (1995)	1.5 – 1.7	3.9 – 4.1	137 - 223	$1.1 \cdot 10^{-4}$	Black Hills Quartzite d = 100 µm	0.15 wt% H_2O added
Hirth et al. (2001)	-	4	135	$6.3 \cdot 10^{-12}$	Fitted flow law experimental / natural	-
Rutter & Brodie (2004a)	0.3	2.97	224	$1.17 \cdot 10^{-5}$	Synthetic d = 12 - 20 µm	0.6 wt%
Rutter & Brodie (2004b)	0.3	1	220	0.4	Synthetic d = 0.4, 1.3, 4.5 µm	0.6 wt%
This Study	1.5	1.8 - 2.0	168 - 170	$3.1 \cdot 10^{-4}$	Crushed Quartz d < 100 µm	0.2 wt% H_2O added

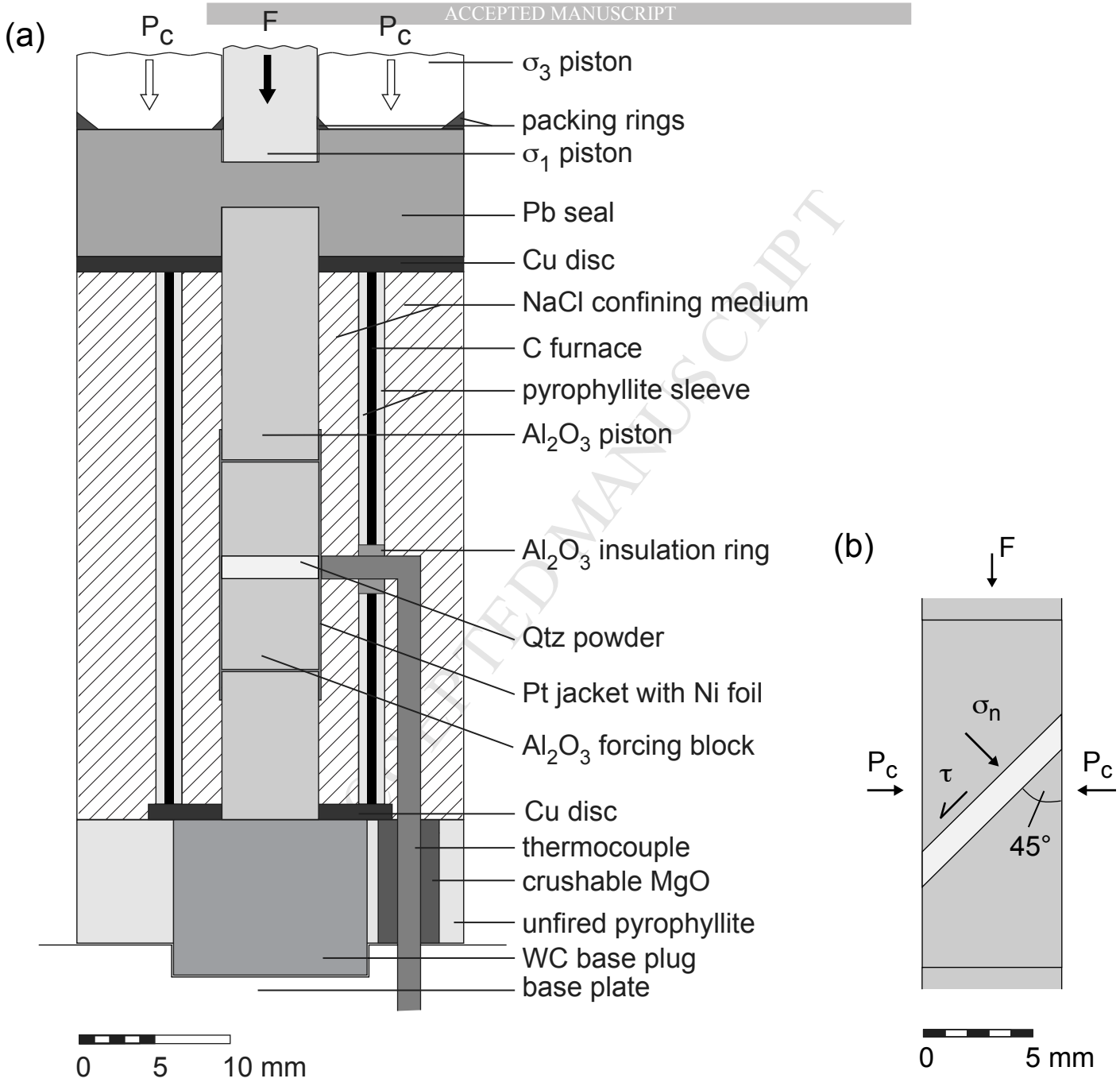

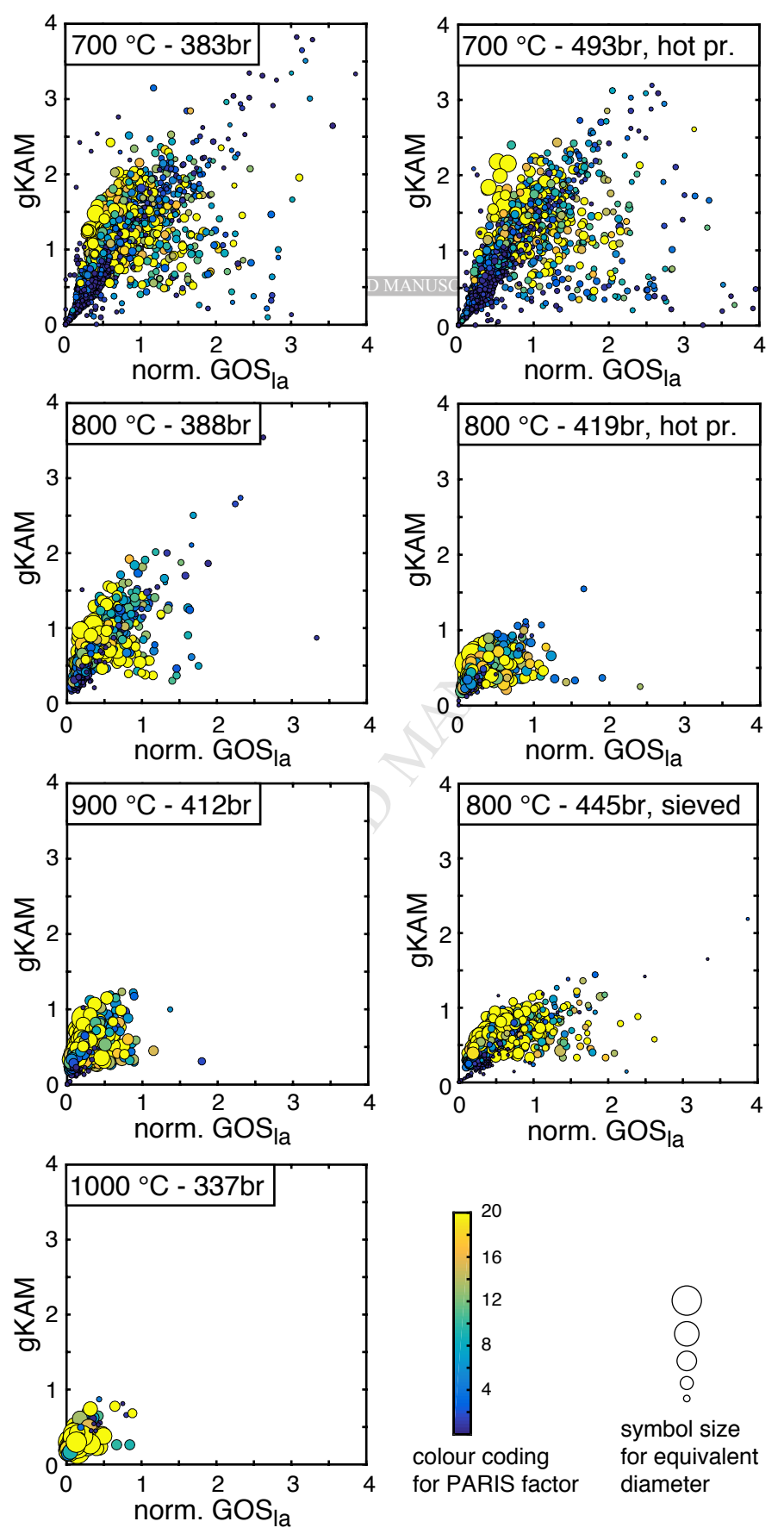
700 °C - 383br
700 °C - 493br, hot pr.
800 °C - 388br
800 °C - 419br, hot pr.
900 °C - 412br
800 °C - 445br, sieved
1000 °C - 337br
gKAM
norm. GOS$_{la}$
0
1
2
3
4
20
16
12
8
4
colour coding
for PARIS factor
symbol size
for equivalent
diameter

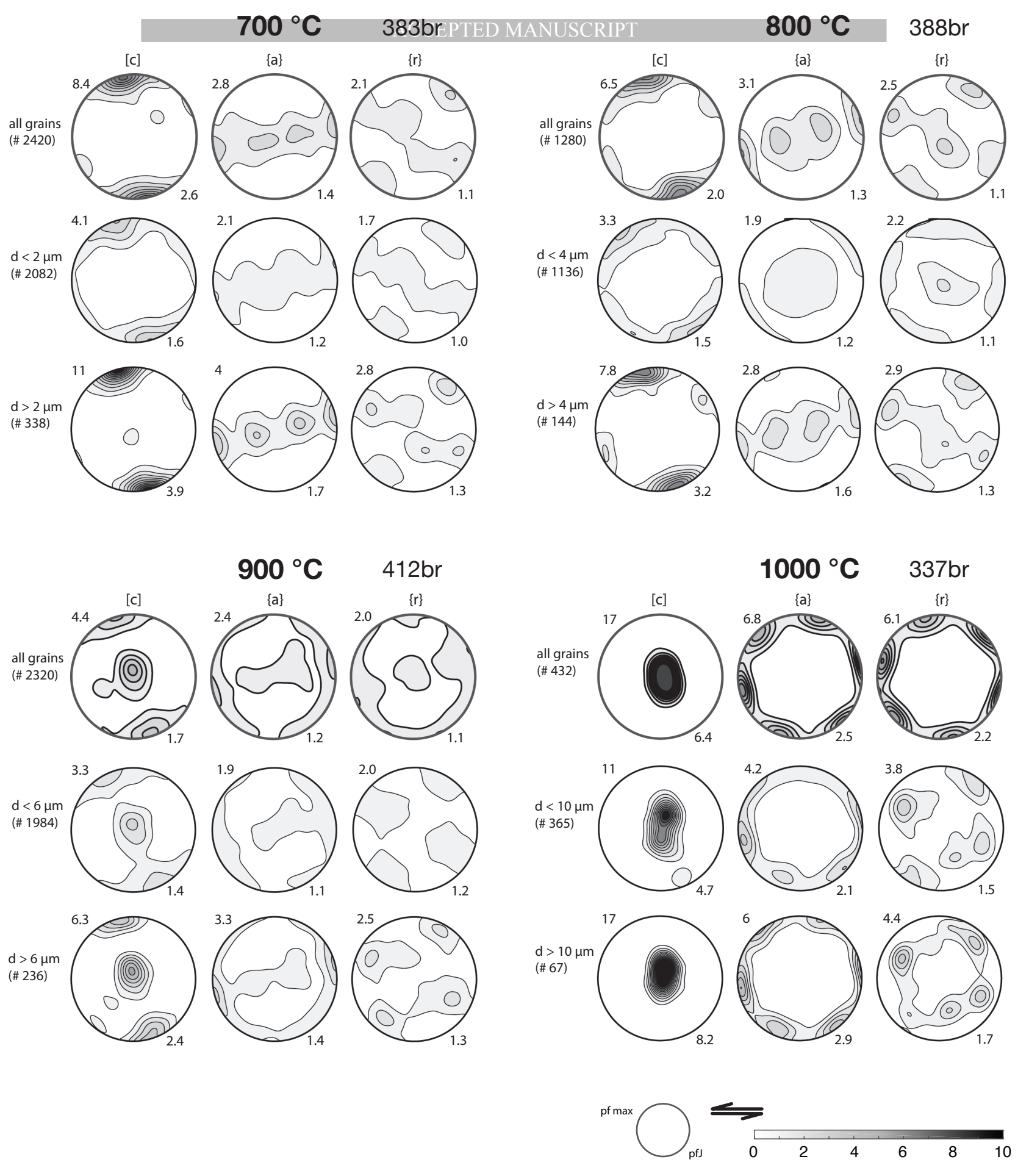

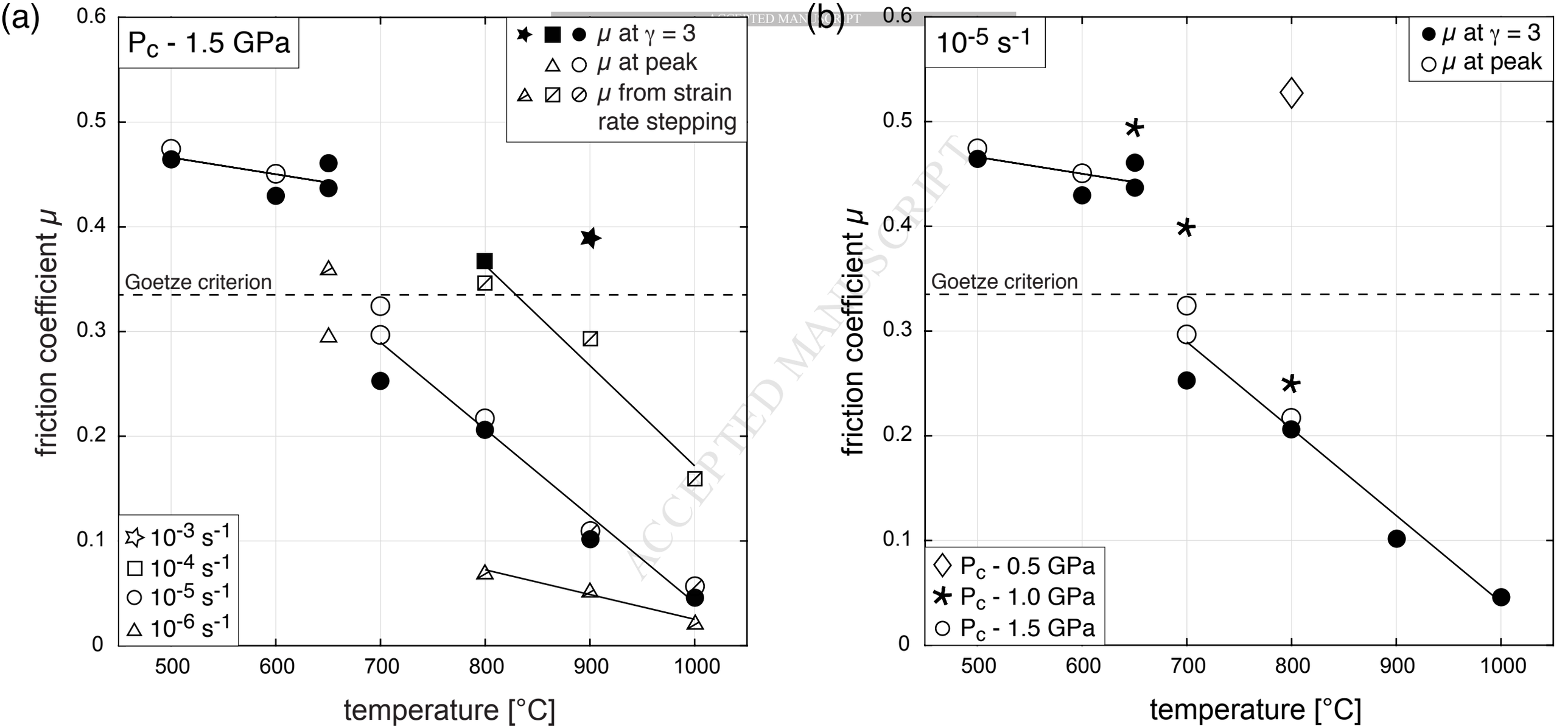

(a)

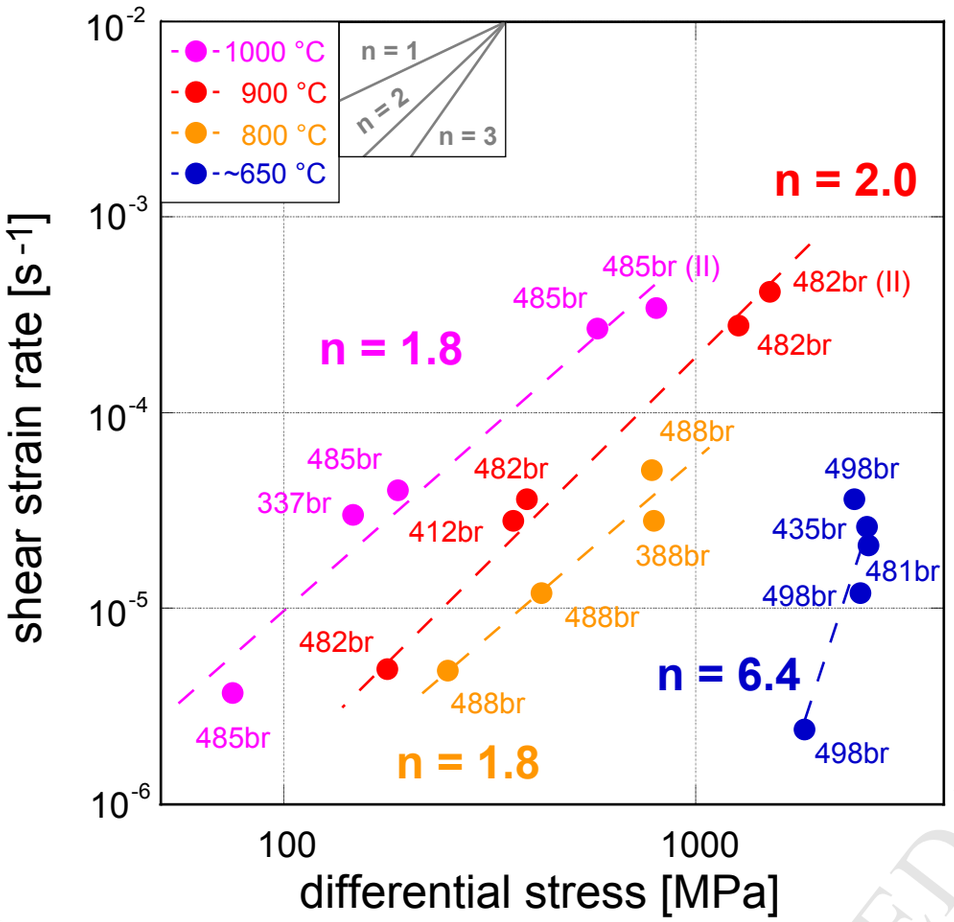

(b)

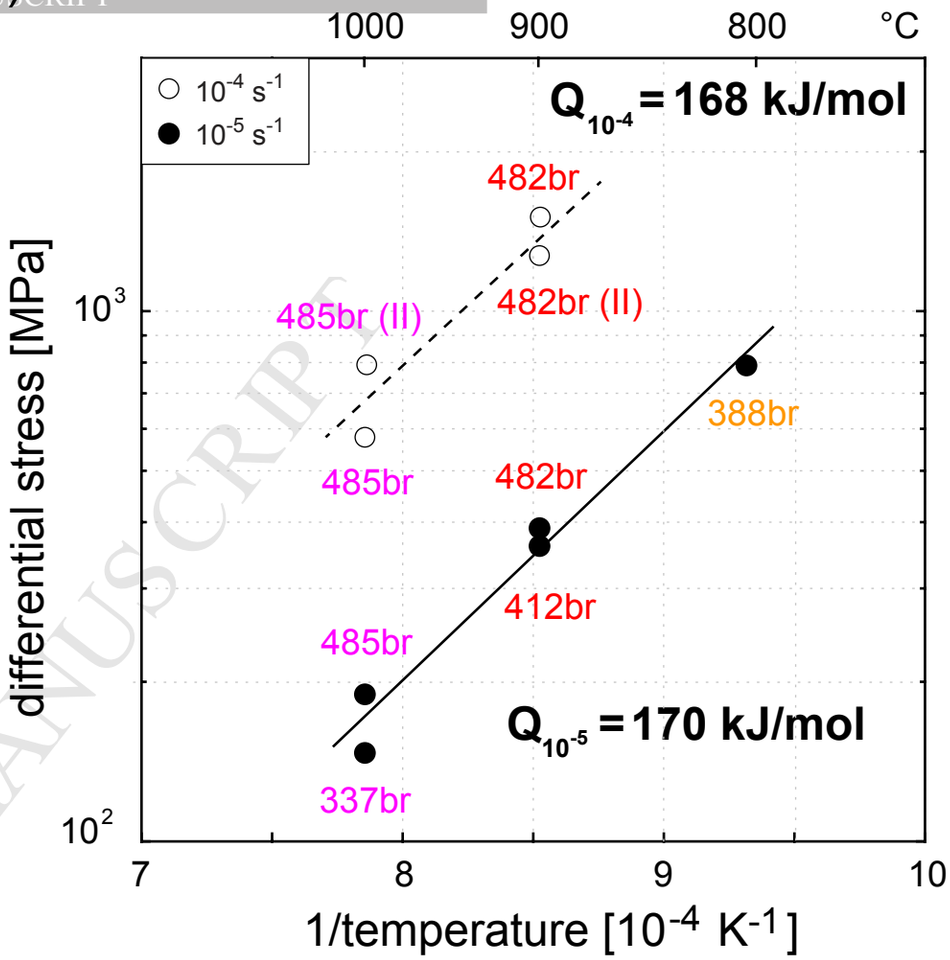

(c)

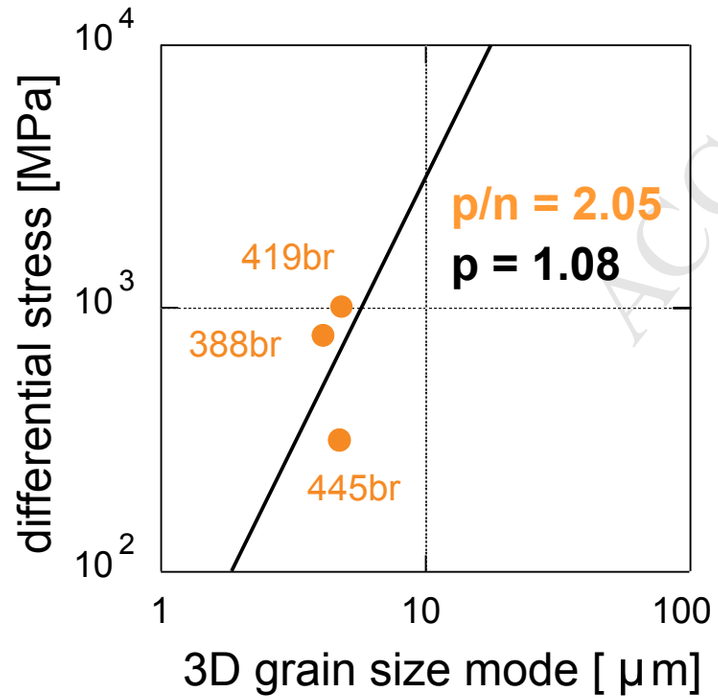

(a)

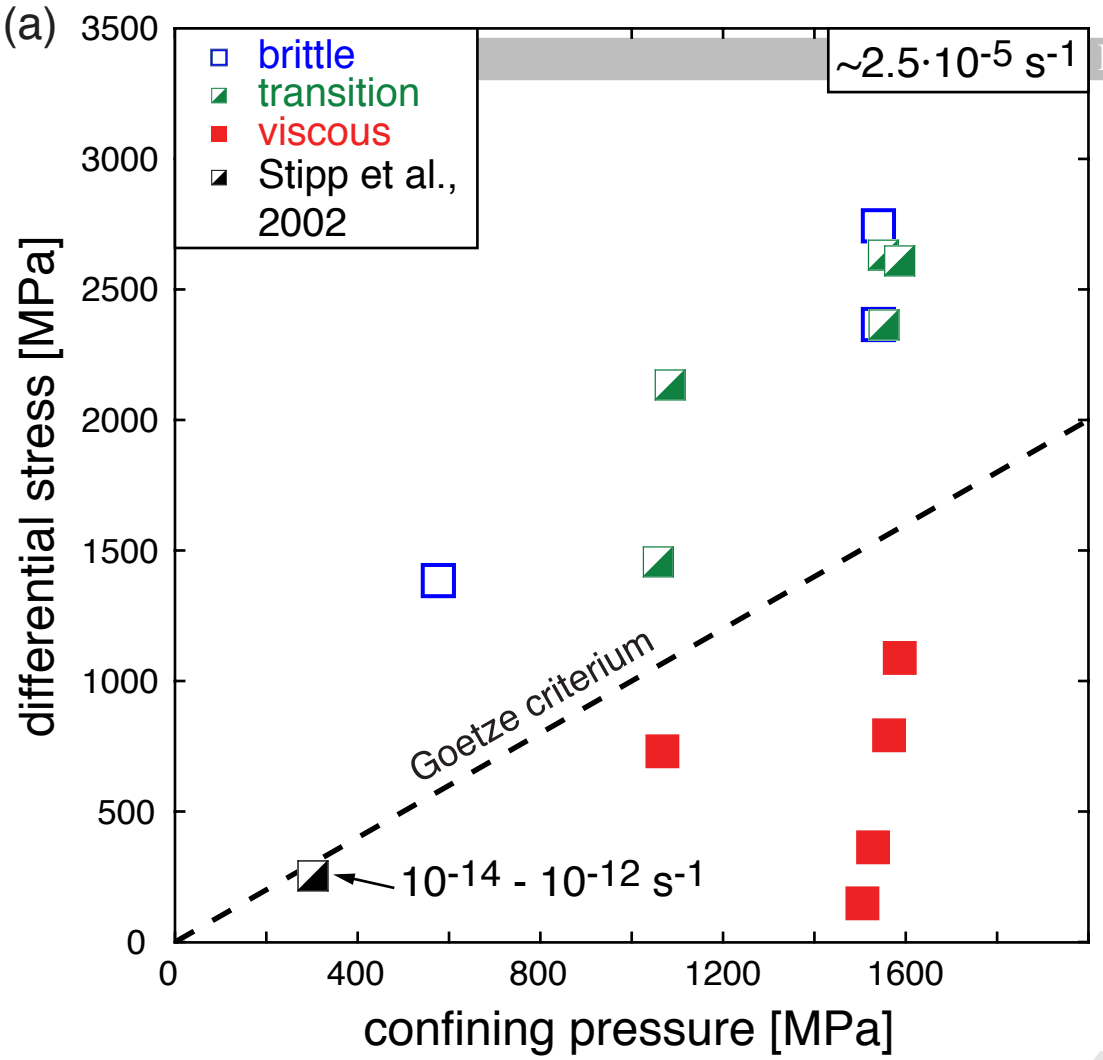

(b)

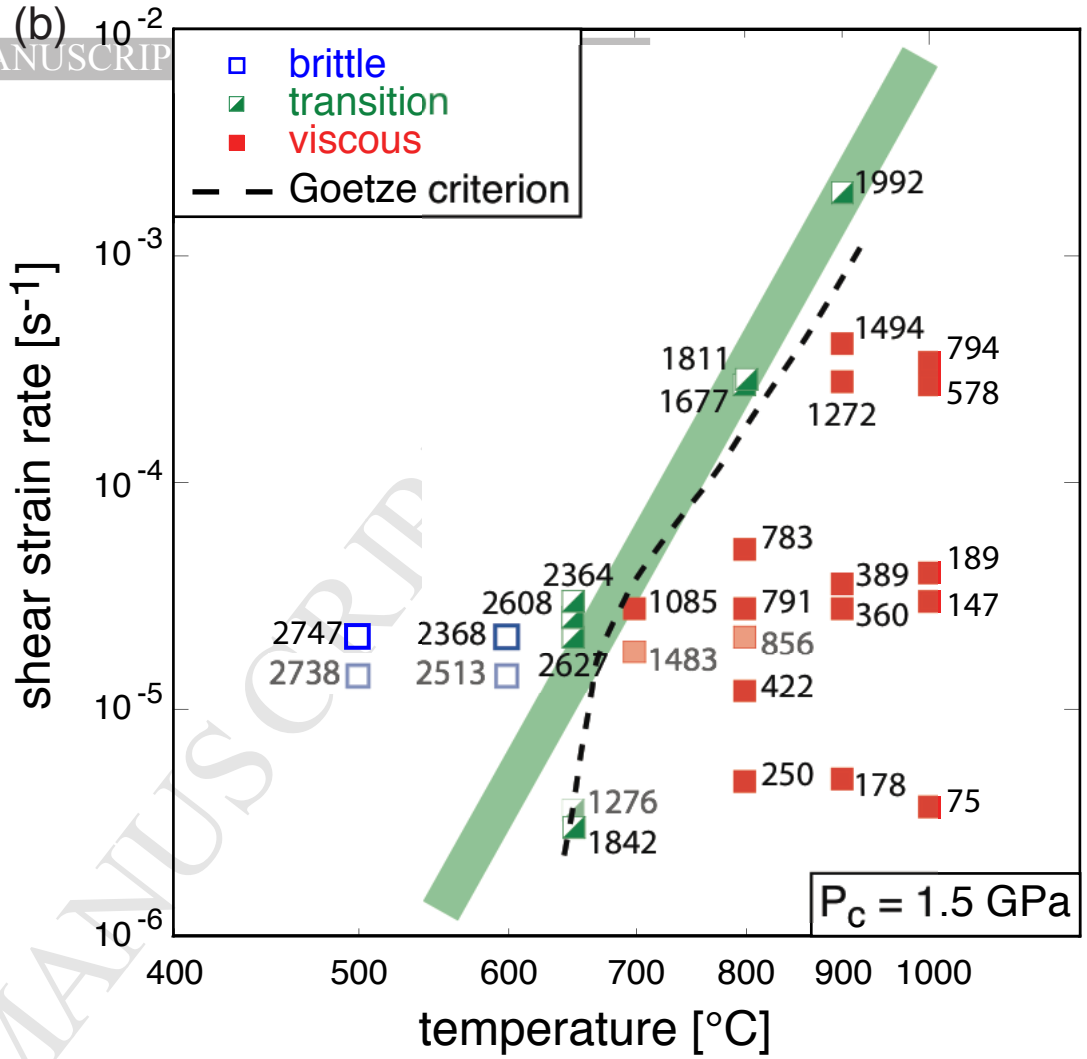

(c)

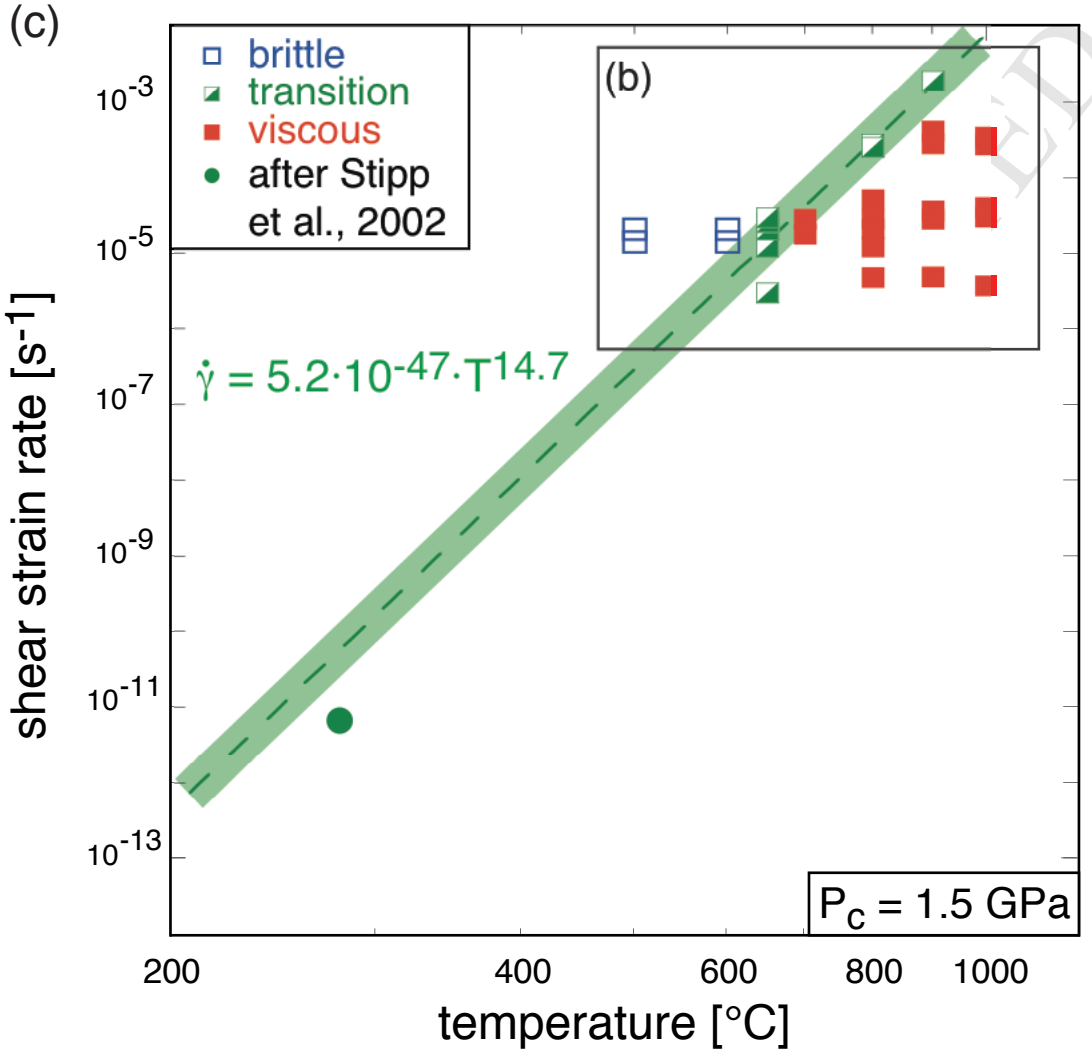

(d)

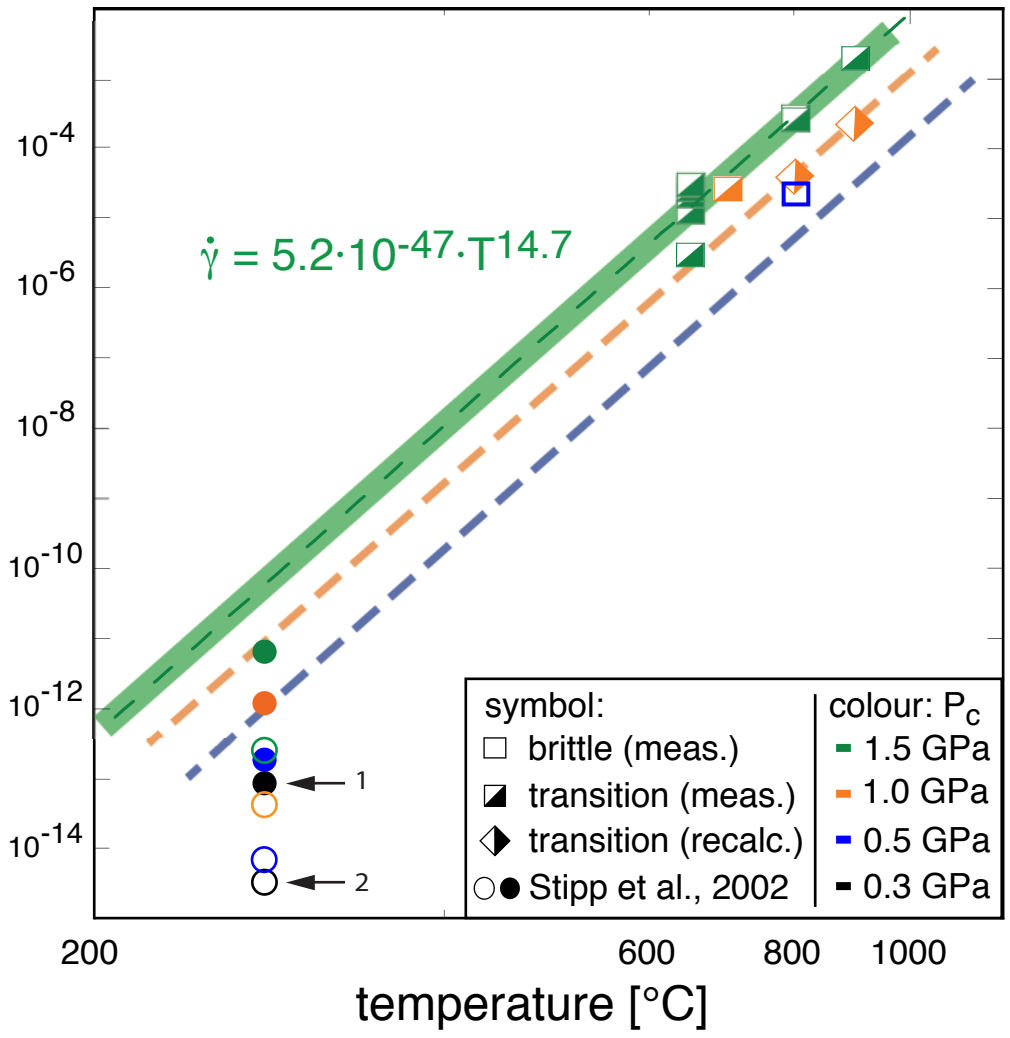

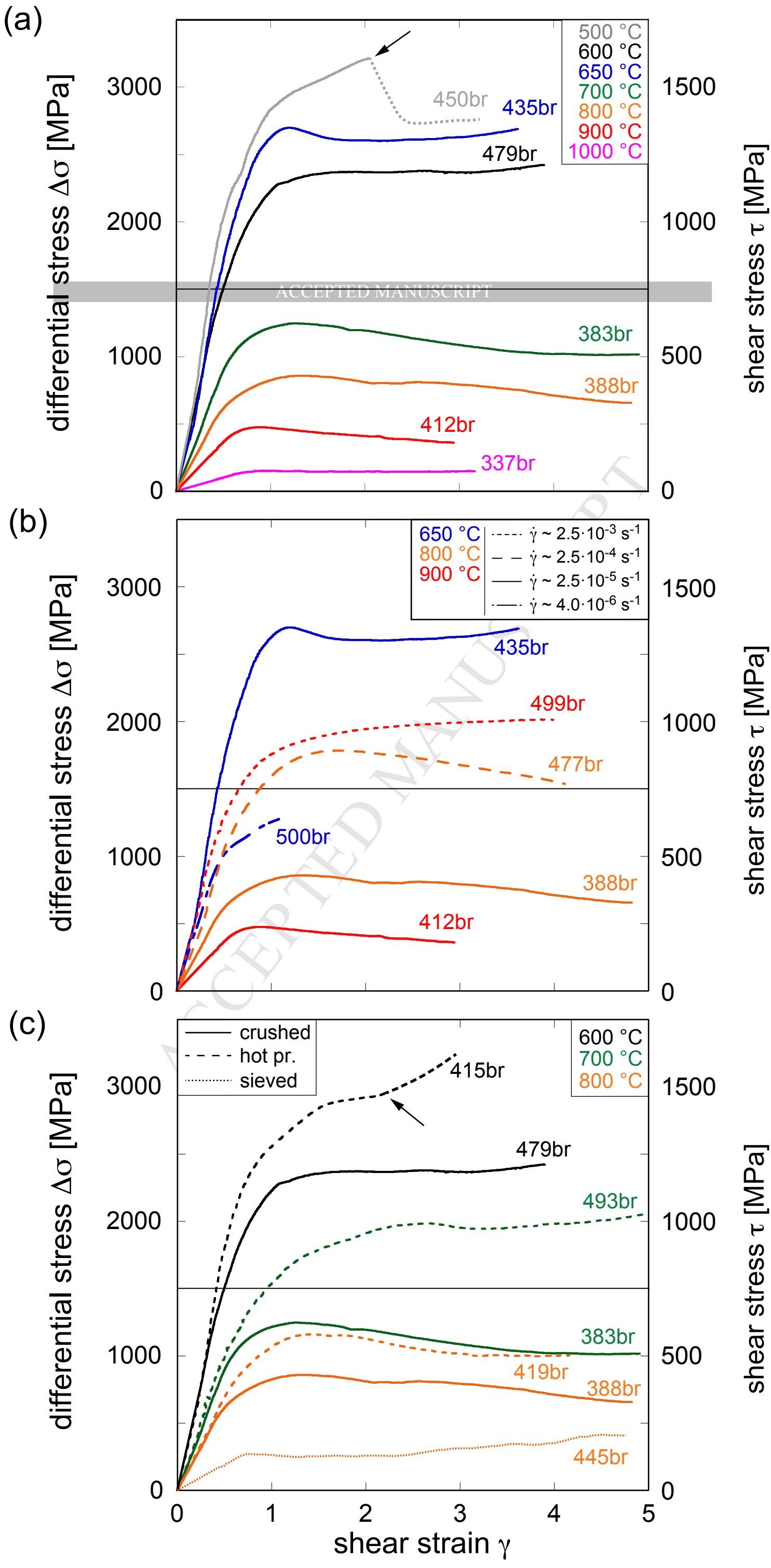

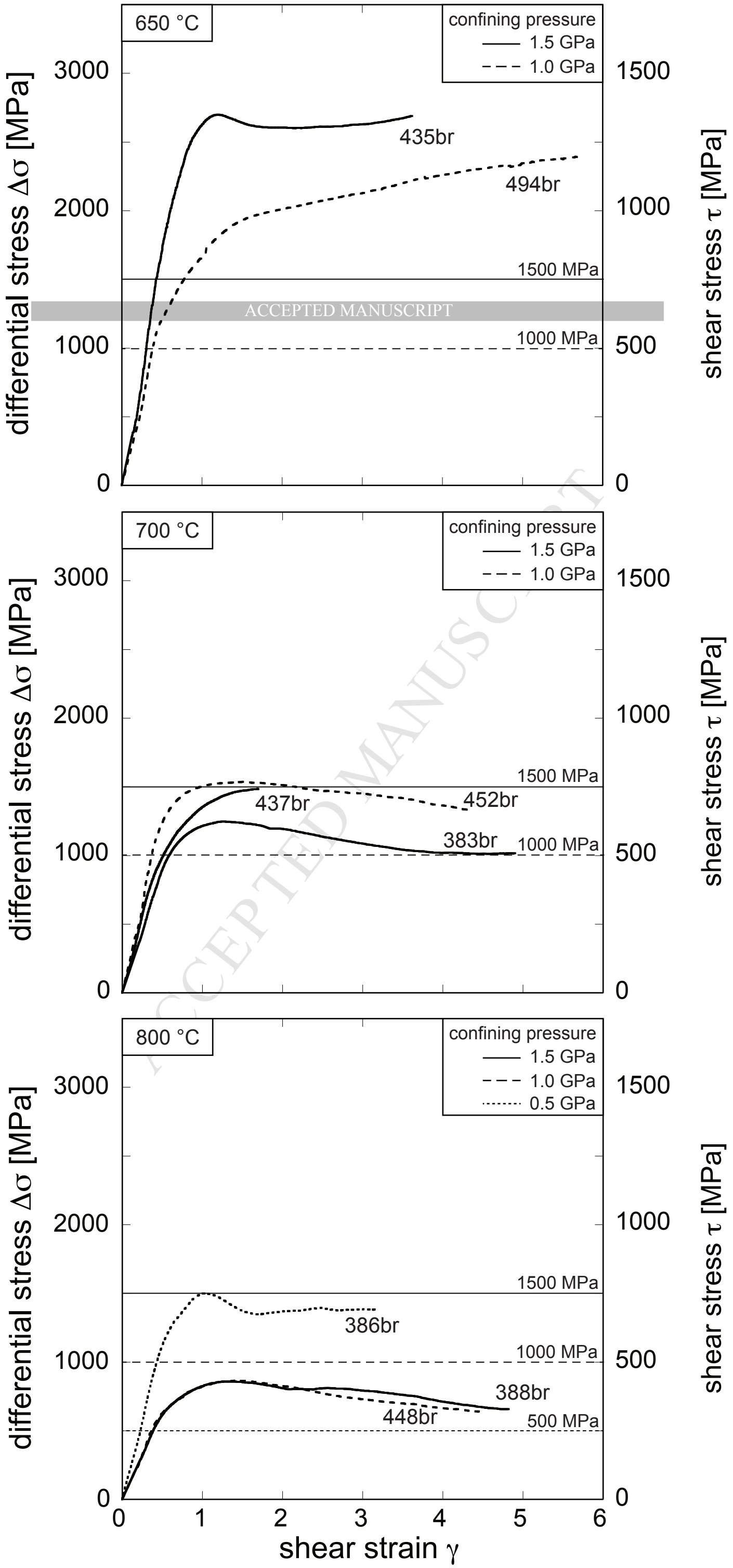

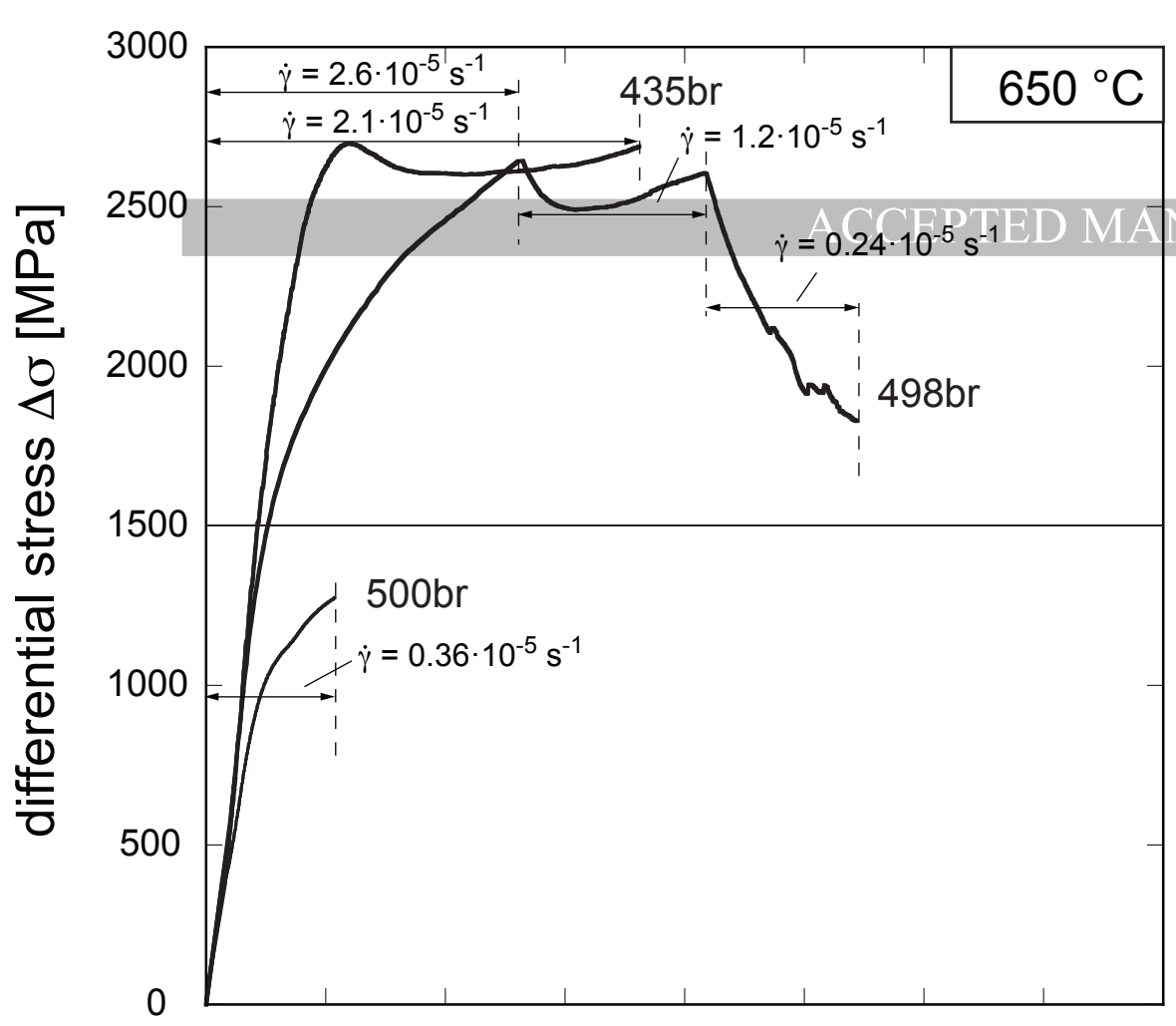

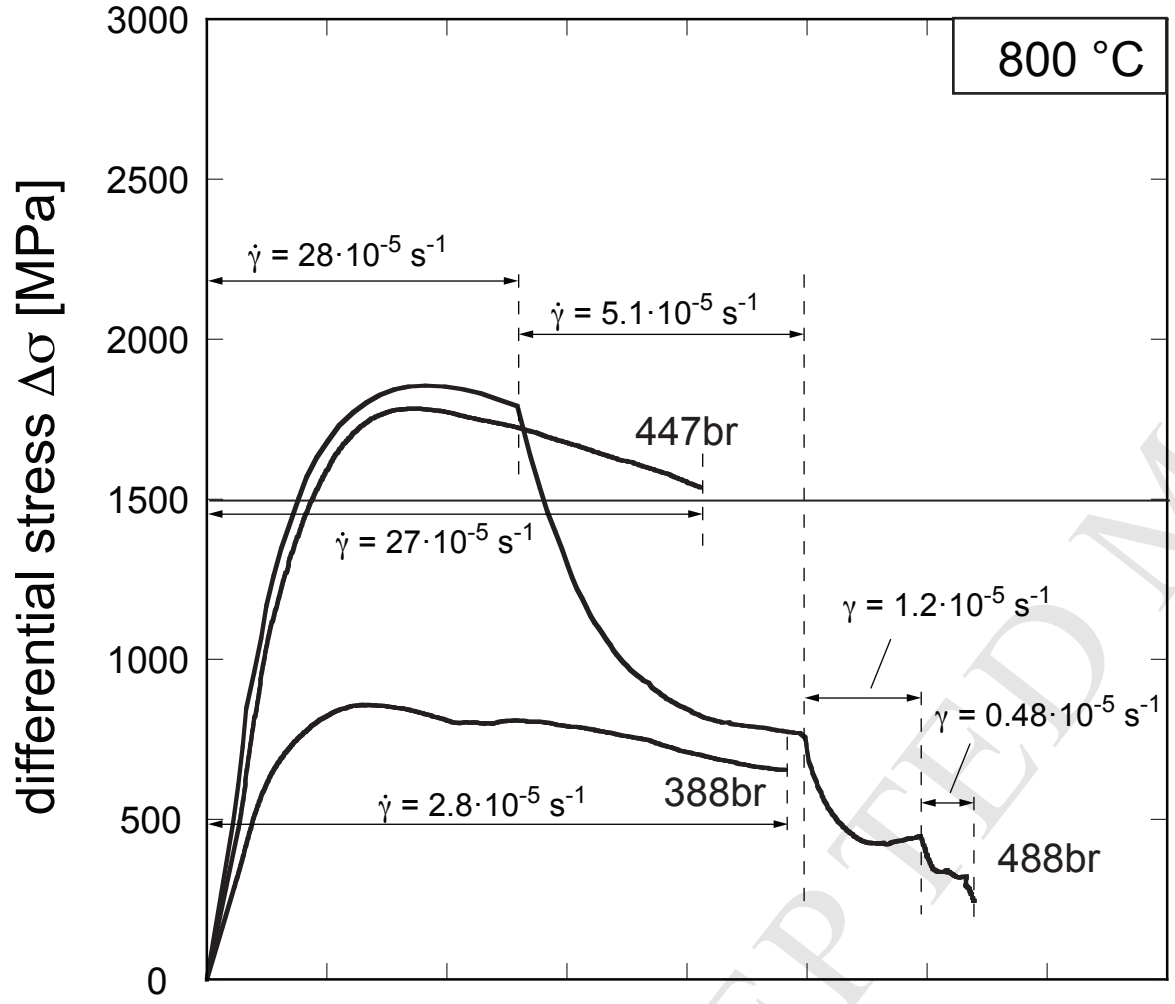

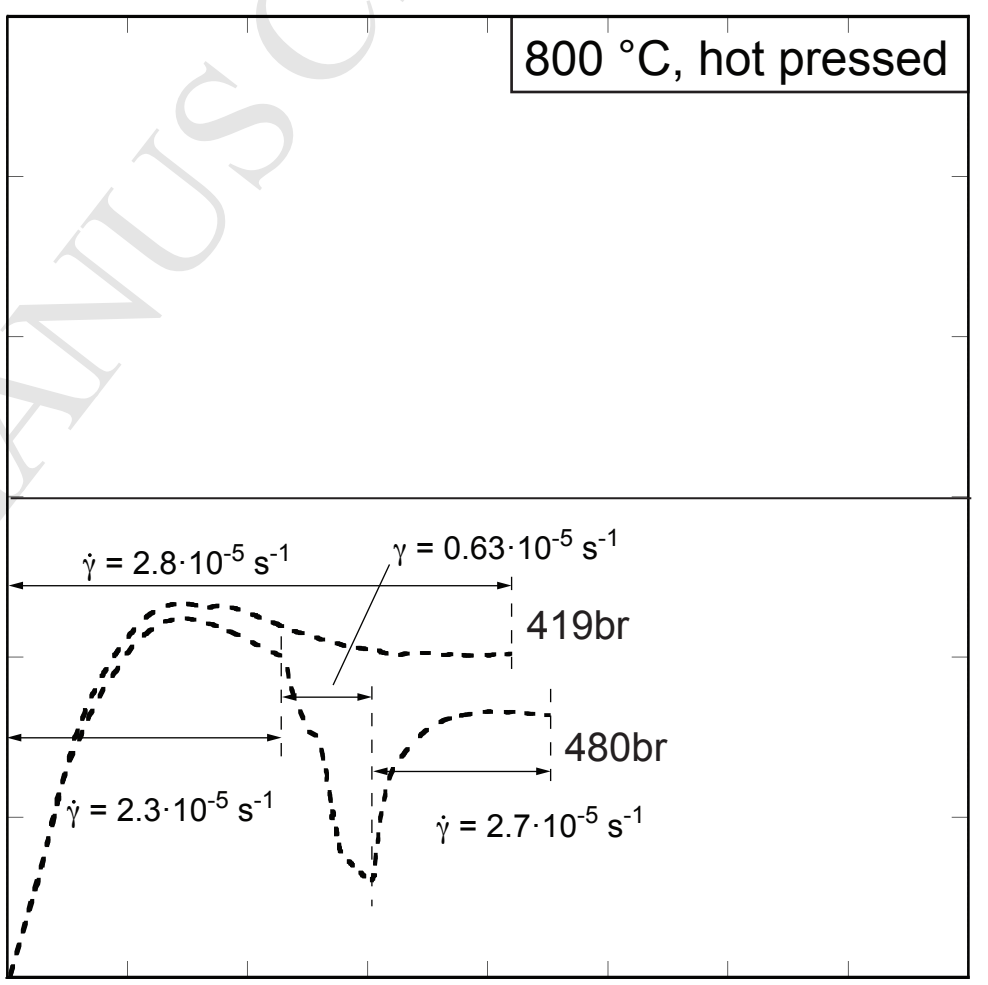

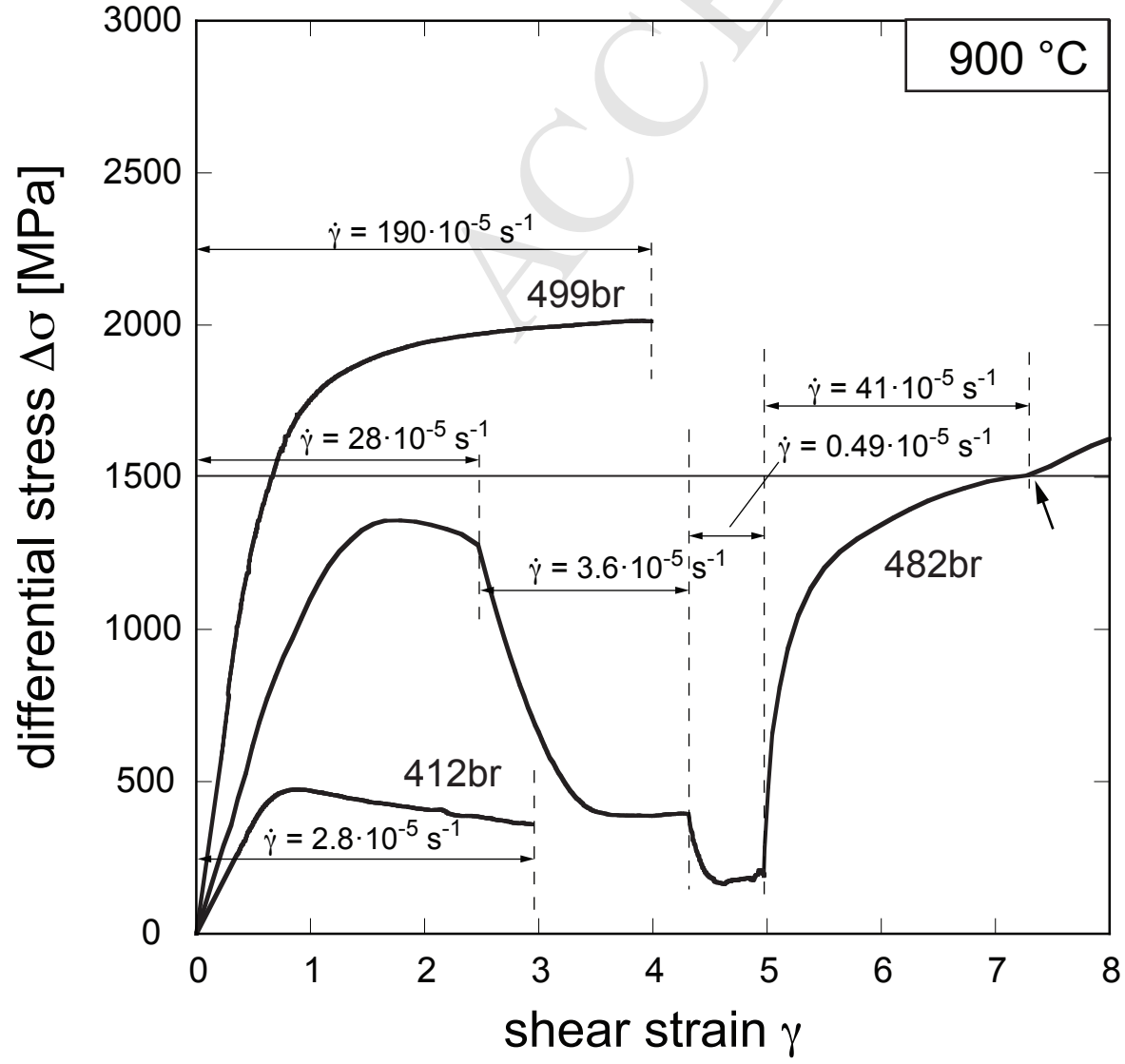

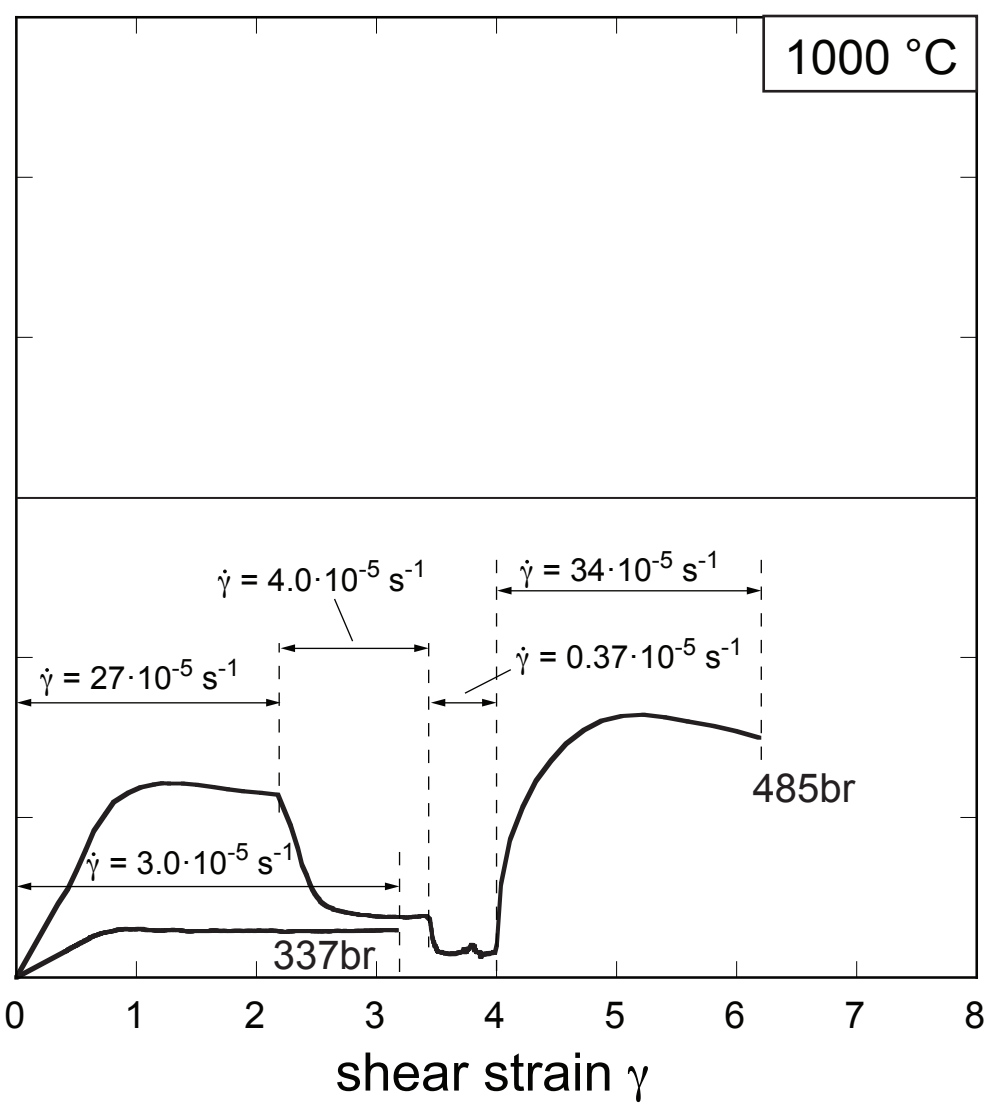

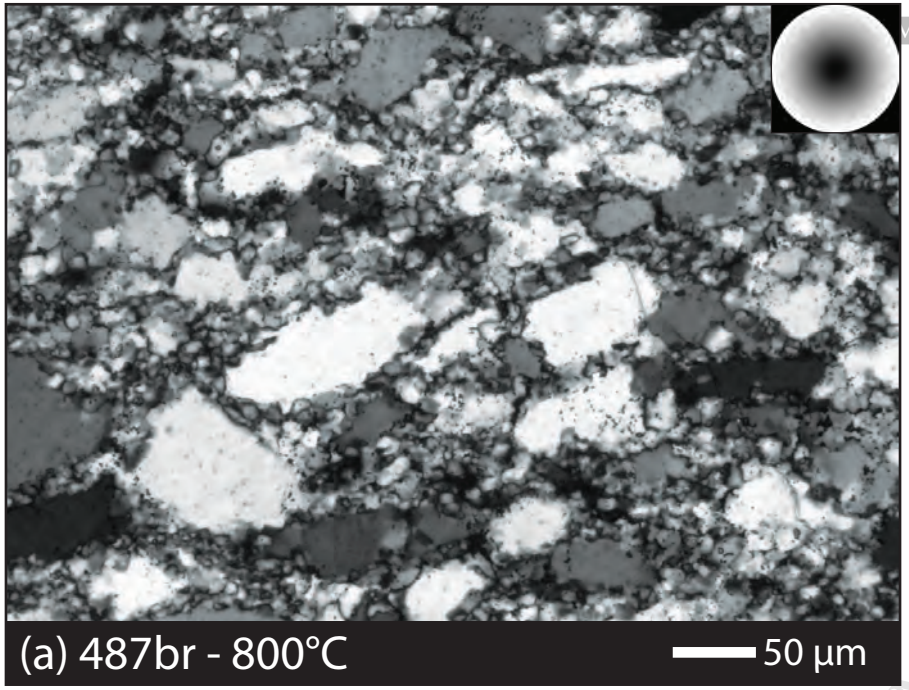
(a) 487br - 800°C
50 µm

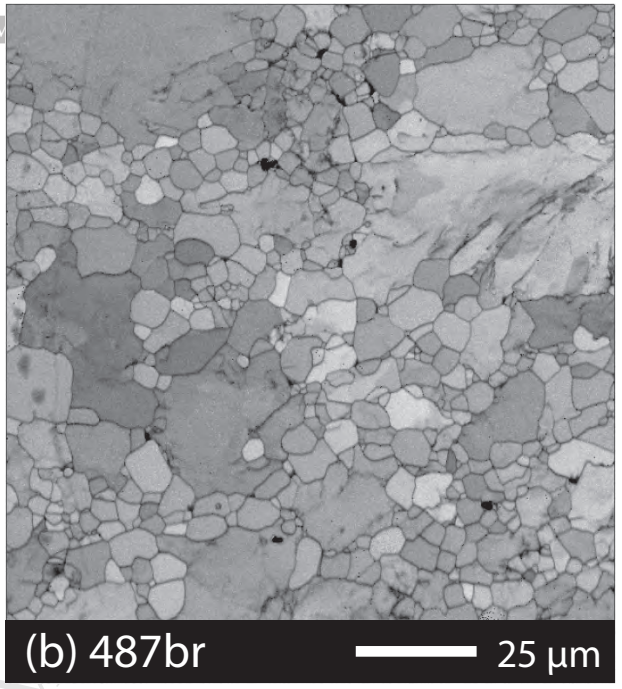
(b) 487br
25 µm

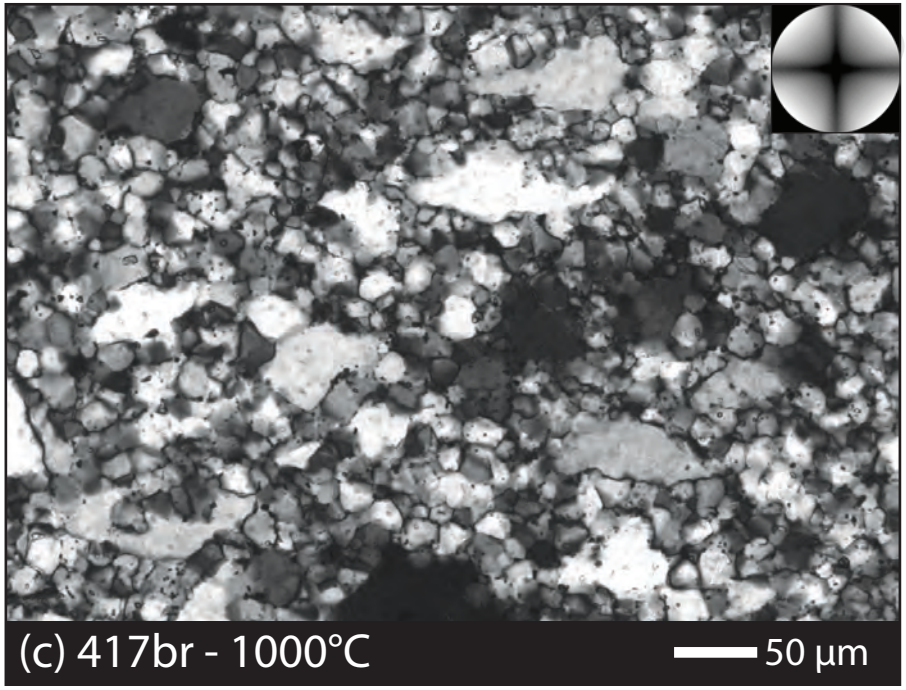
(c) 417br - 1000°C
50 µm

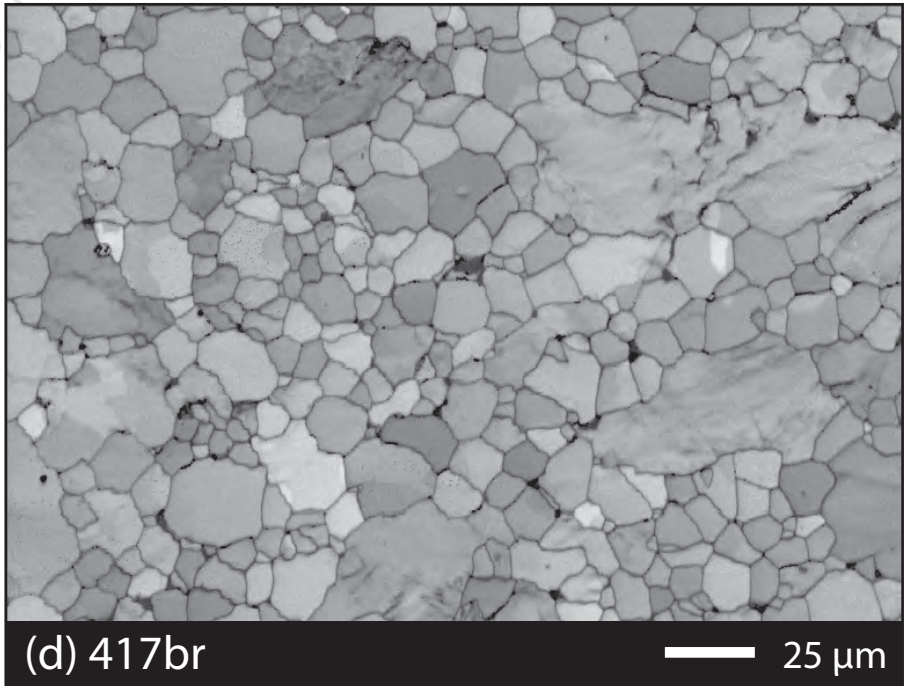
(d) 417br
25 µm

crushed

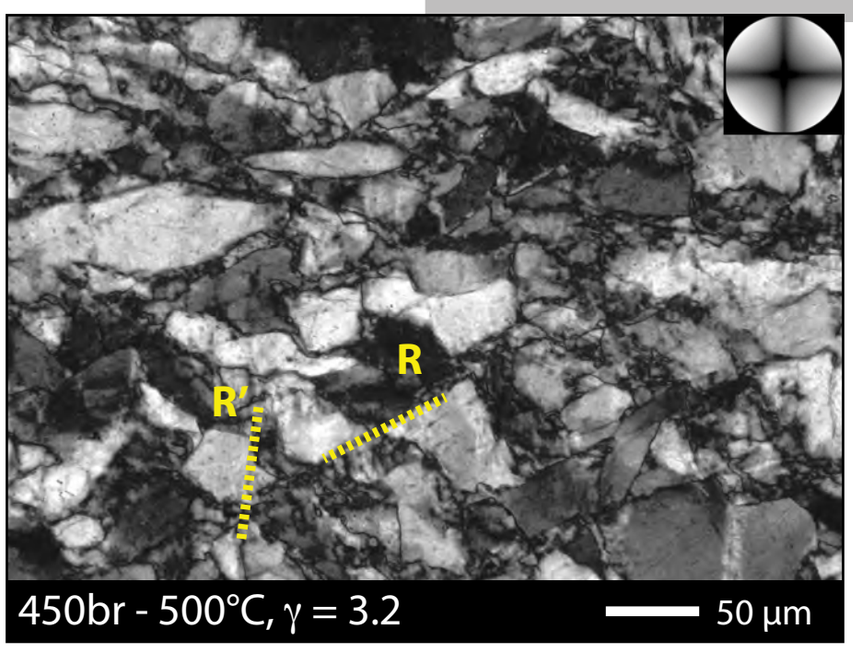

450br - 500°C, γ = 3.2 — 50 µm

crushed

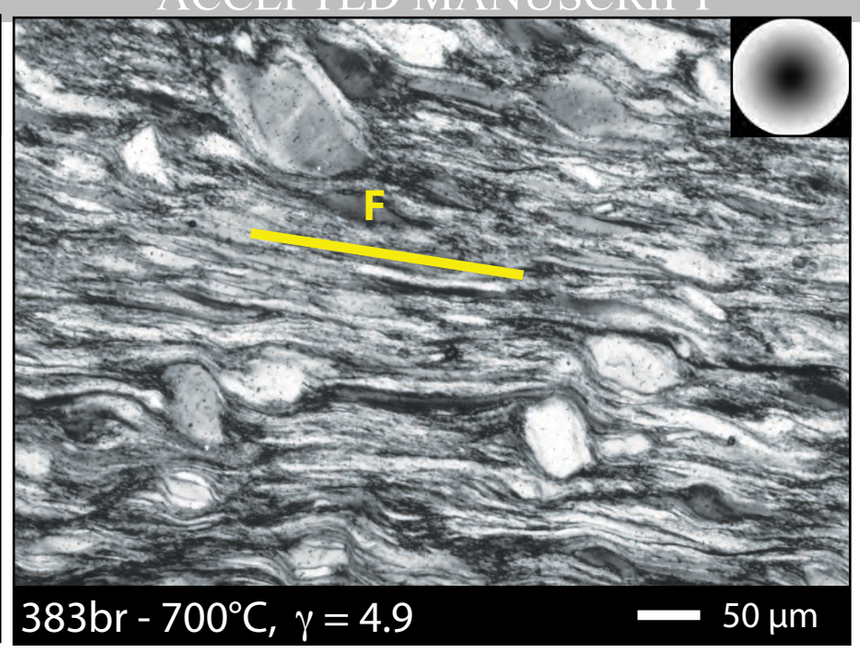

383br - 700°C, γ = 4.9 — 50 µm

hot pressed

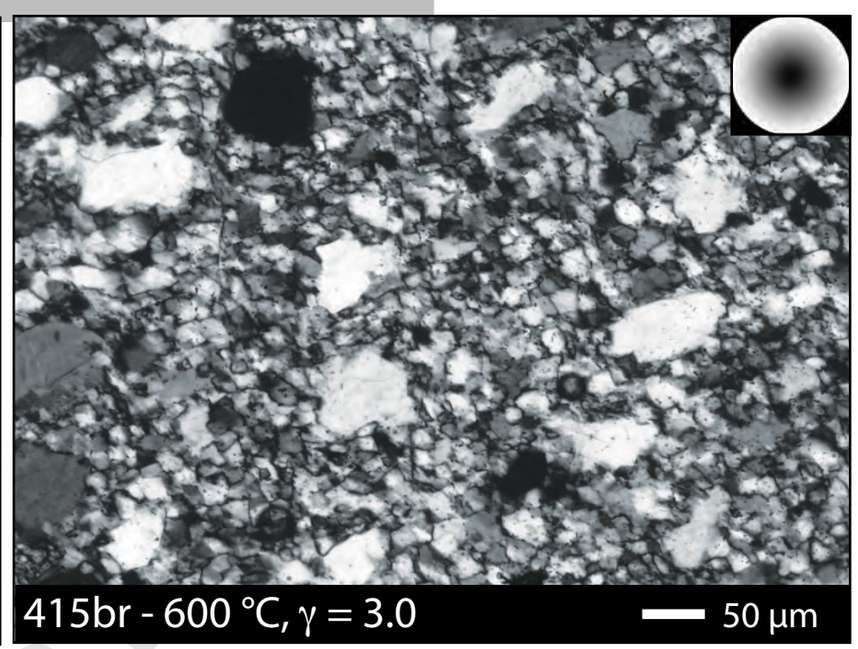

415br - 600 °C, γ = 3.0 — 50 µm

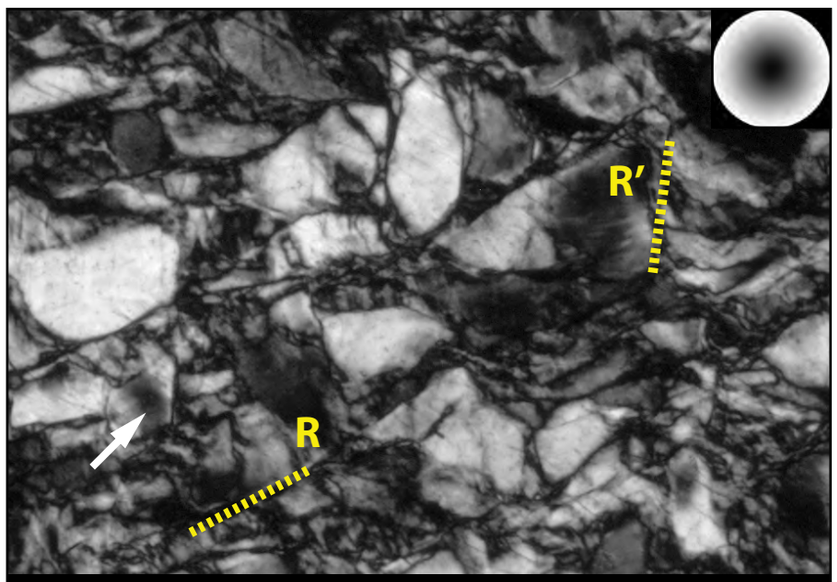

479br - 600°C, γ = 3.9 — 50 µm

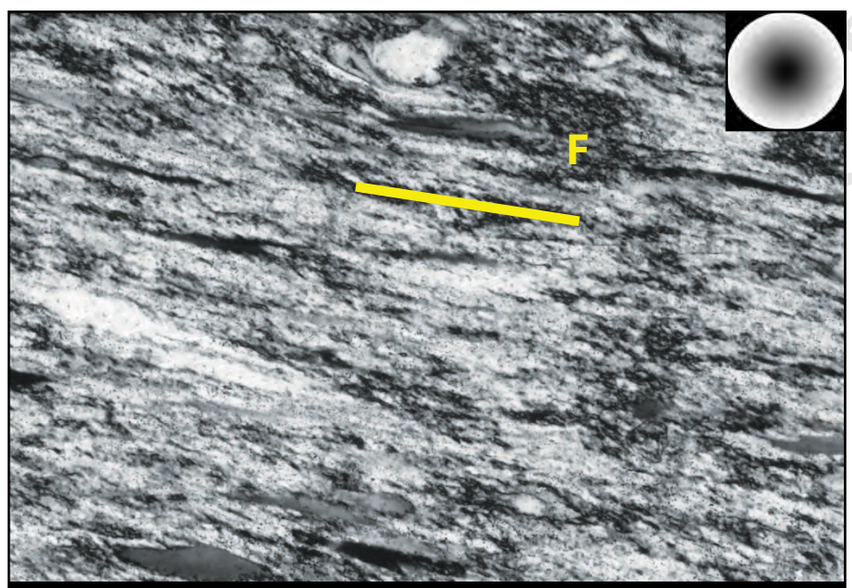

388br - 800°C, γ = 4.8 — 50 µm

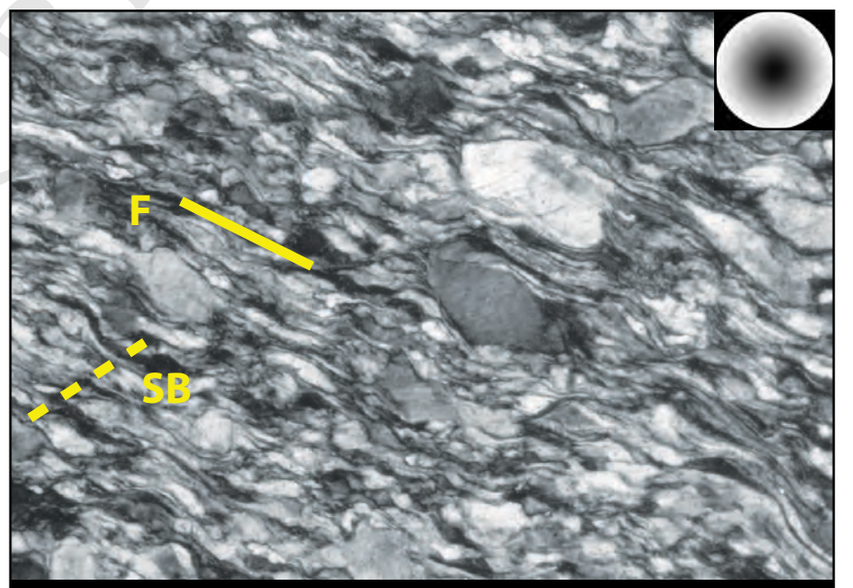

493br - 700 °C, γ = 4.9 — 50 µm

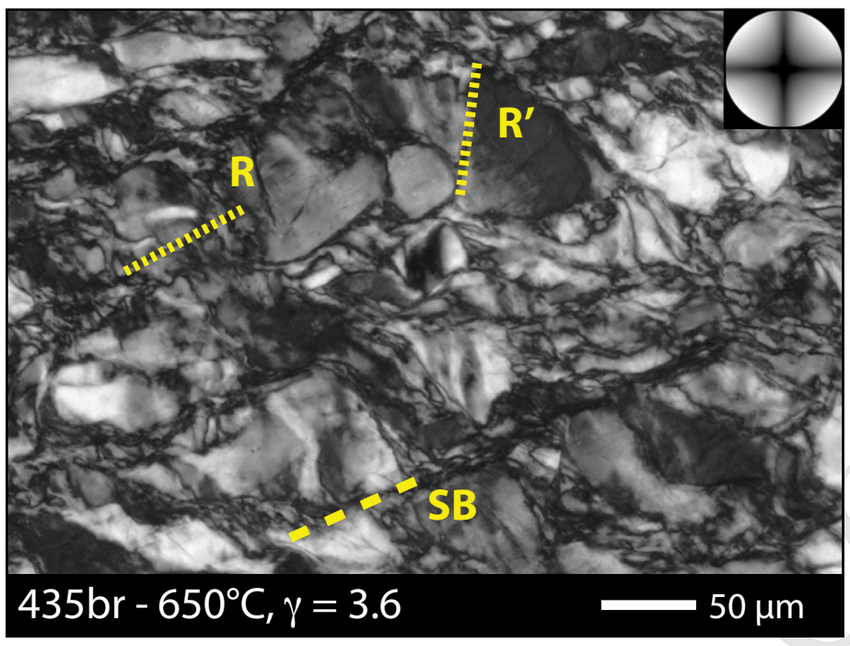

435br - 650°C, γ = 3.6 — 50 µm

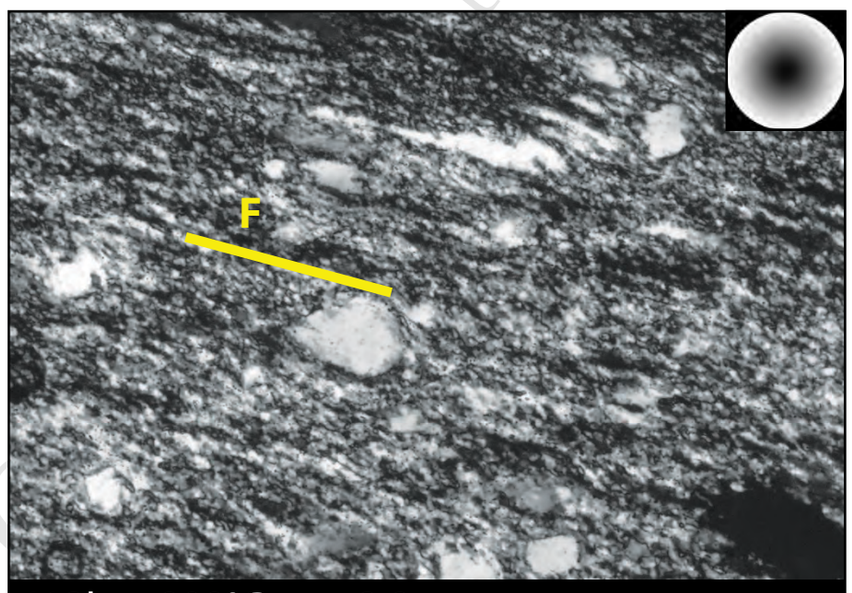

412br - 900°C, γ = 2.9 — 50 µm

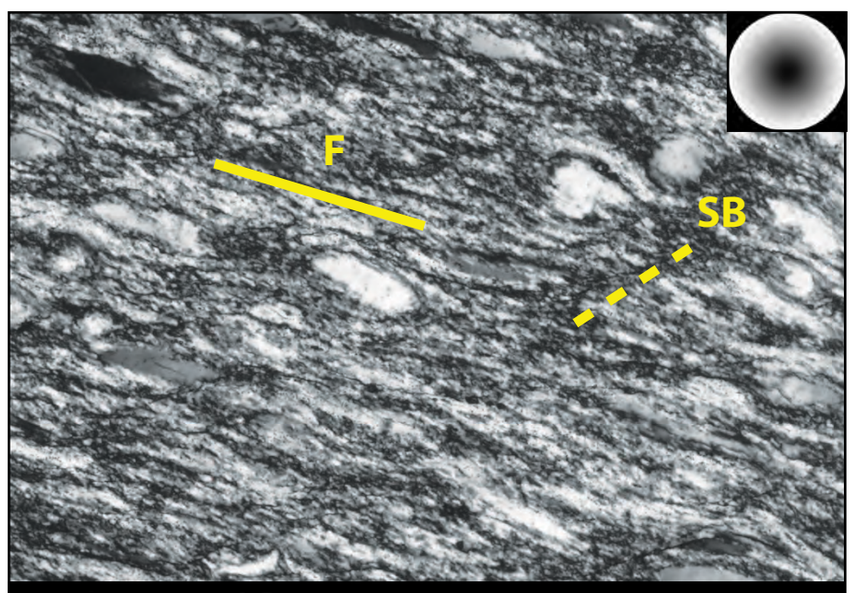

419br - 800 °C, γ = 4.2 — 50 µm

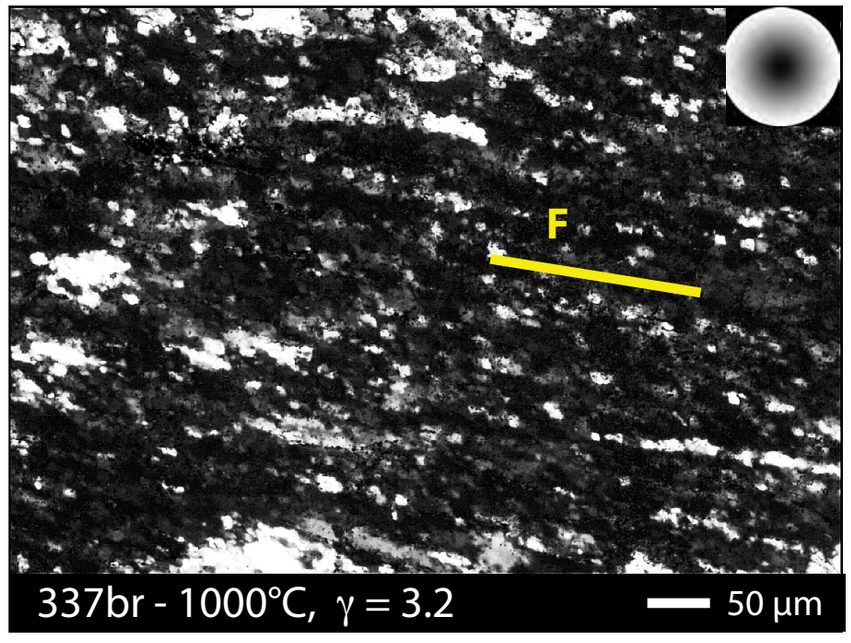

337br - 1000°C, γ = 3.2 — 50 µm

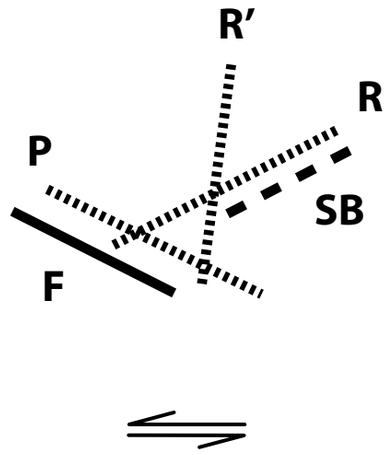

$\dot{\gamma}$ ~ $2.5 \cdot 10^{-5}$ s^{-1}, P_C = 1.0 GPa

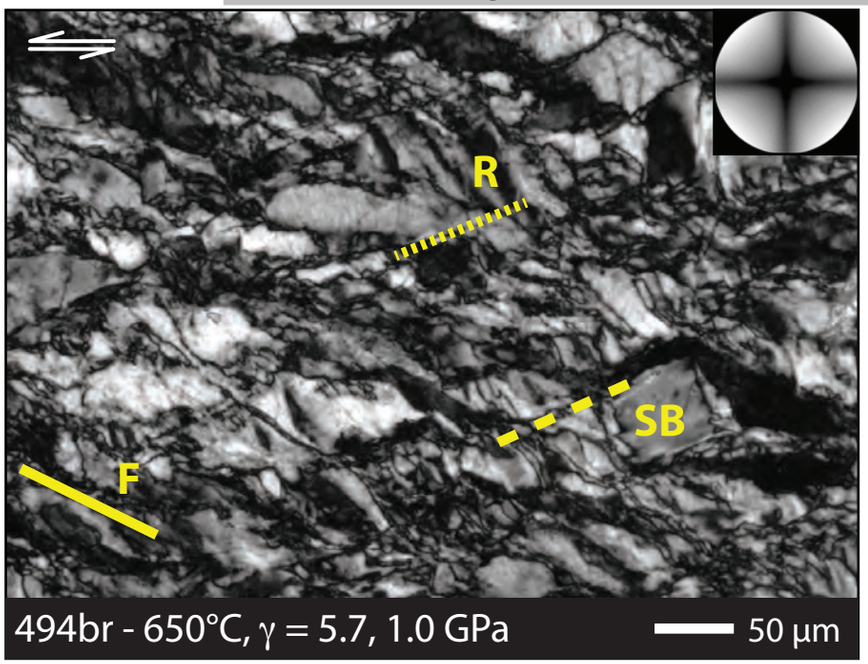

494br - 650°C, γ = 5.7, 1.0 GPa — 50 µm

P_C = 1.5 GPa, various $\dot{\gamma}$

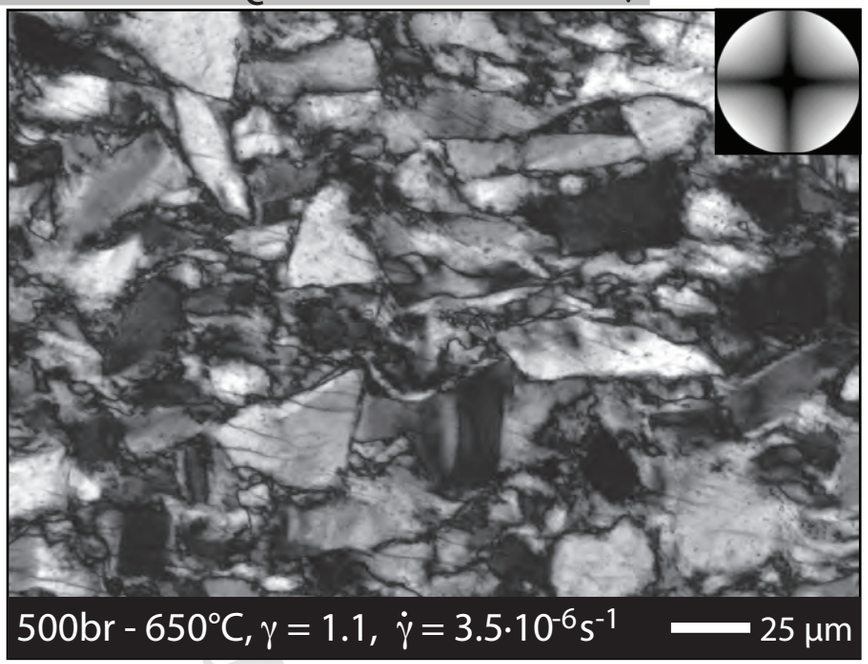

500br - 650°C, γ = 1.1, $\dot{\gamma} = 3.5 \cdot 10^{-6} s^{-1}$ — 25 µm

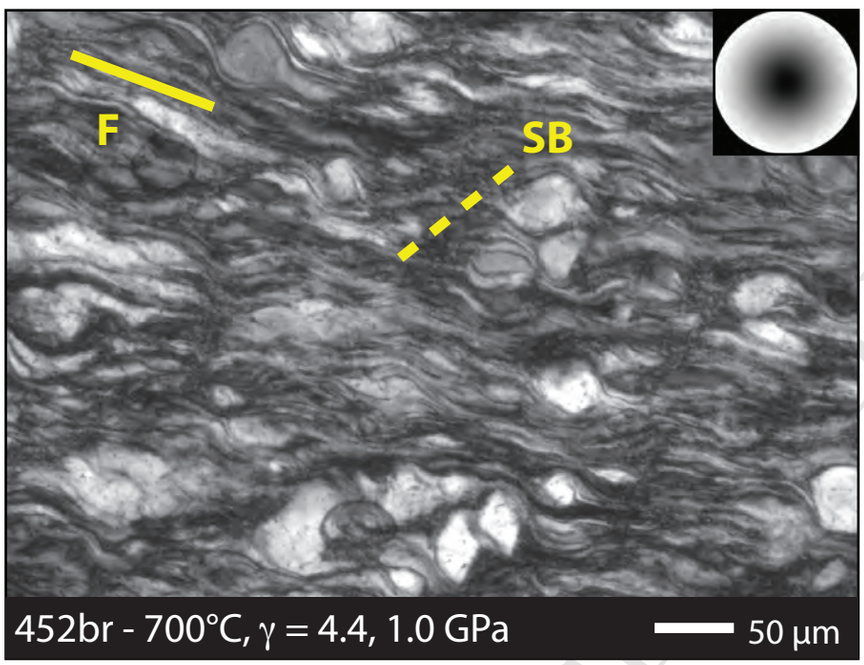

452br - 700°C, γ = 4.4, 1.0 GPa — 50 µm

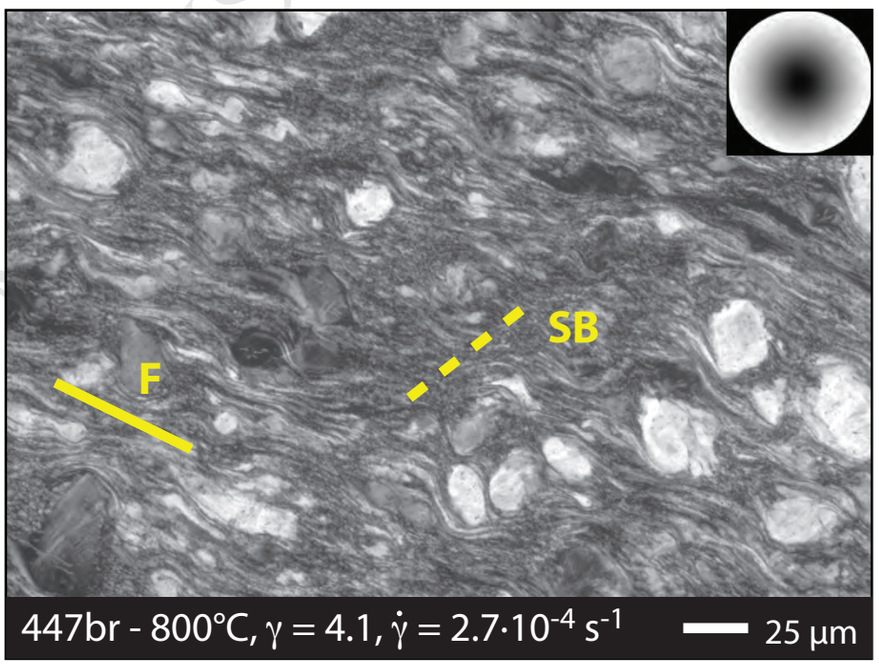

447br - 800°C, γ = 4.1, $\dot{\gamma} = 2.7 \cdot 10^{-4}$ s^{-1} — 25 µm

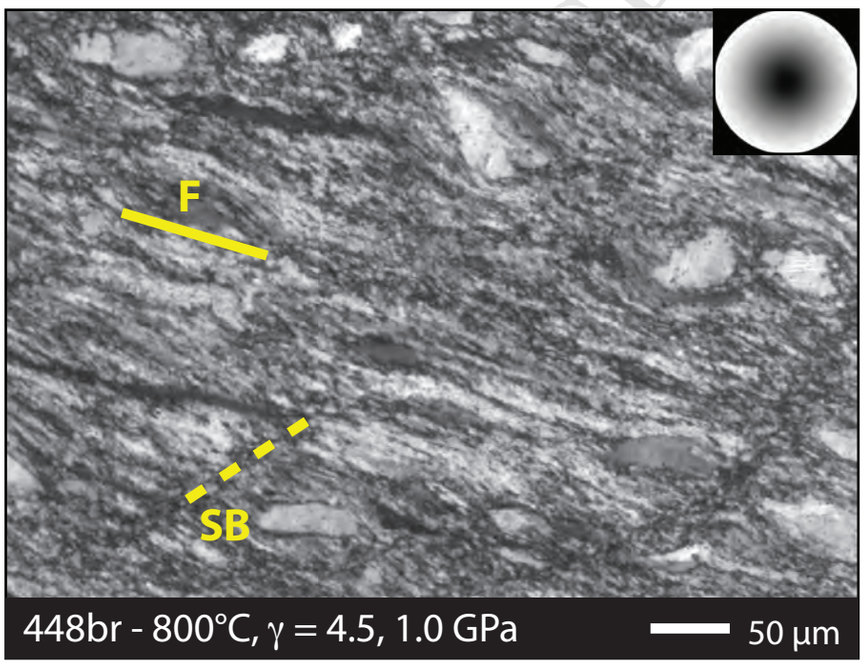

448br - 800°C, γ = 4.5, 1.0 GPa — 50 µm

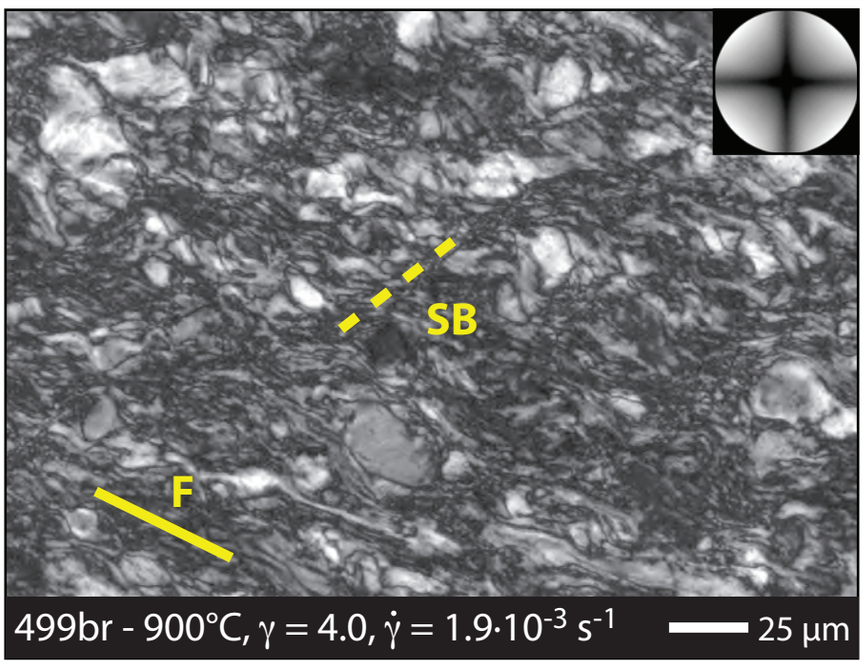

499br - 900°C, γ = 4.0, $\dot{\gamma} = 1.9 \cdot 10^{-3}$ s^{-1} — 25 µm

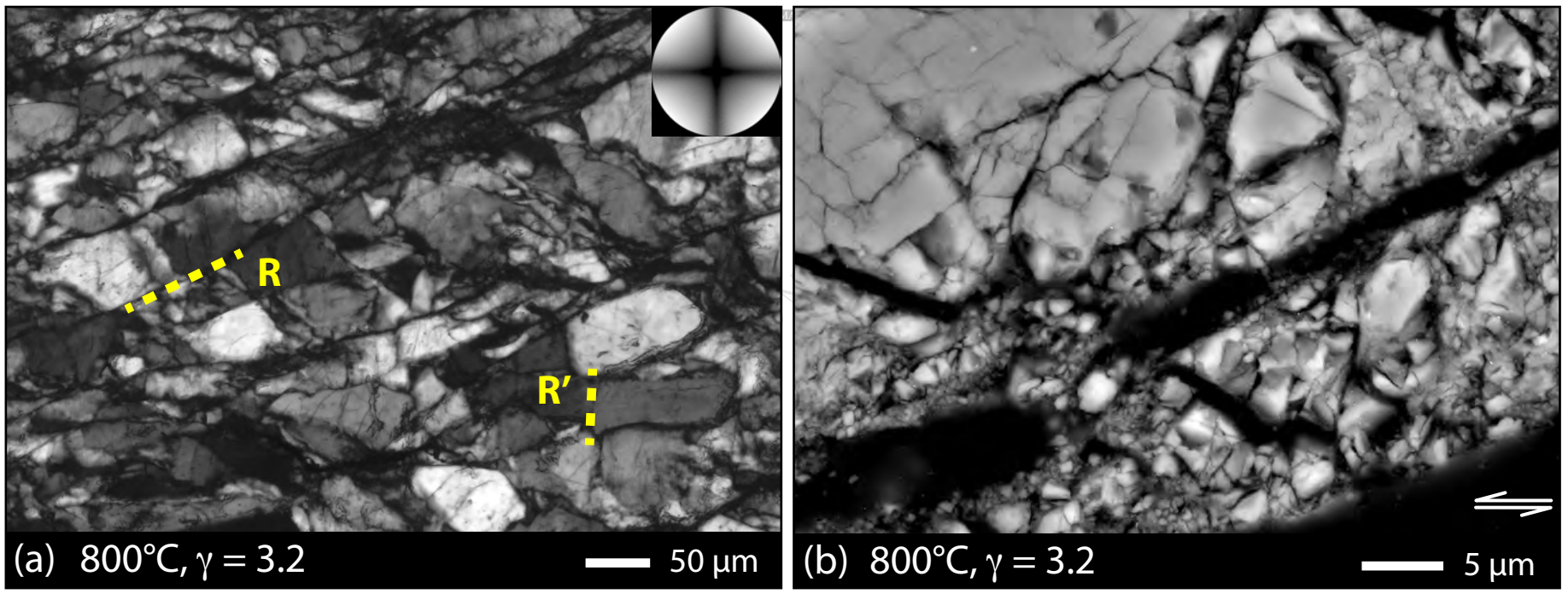
R
R′
(a) 800°C, γ = 3.2
50 μm
(b) 800°C, γ = 3.2
5 μm

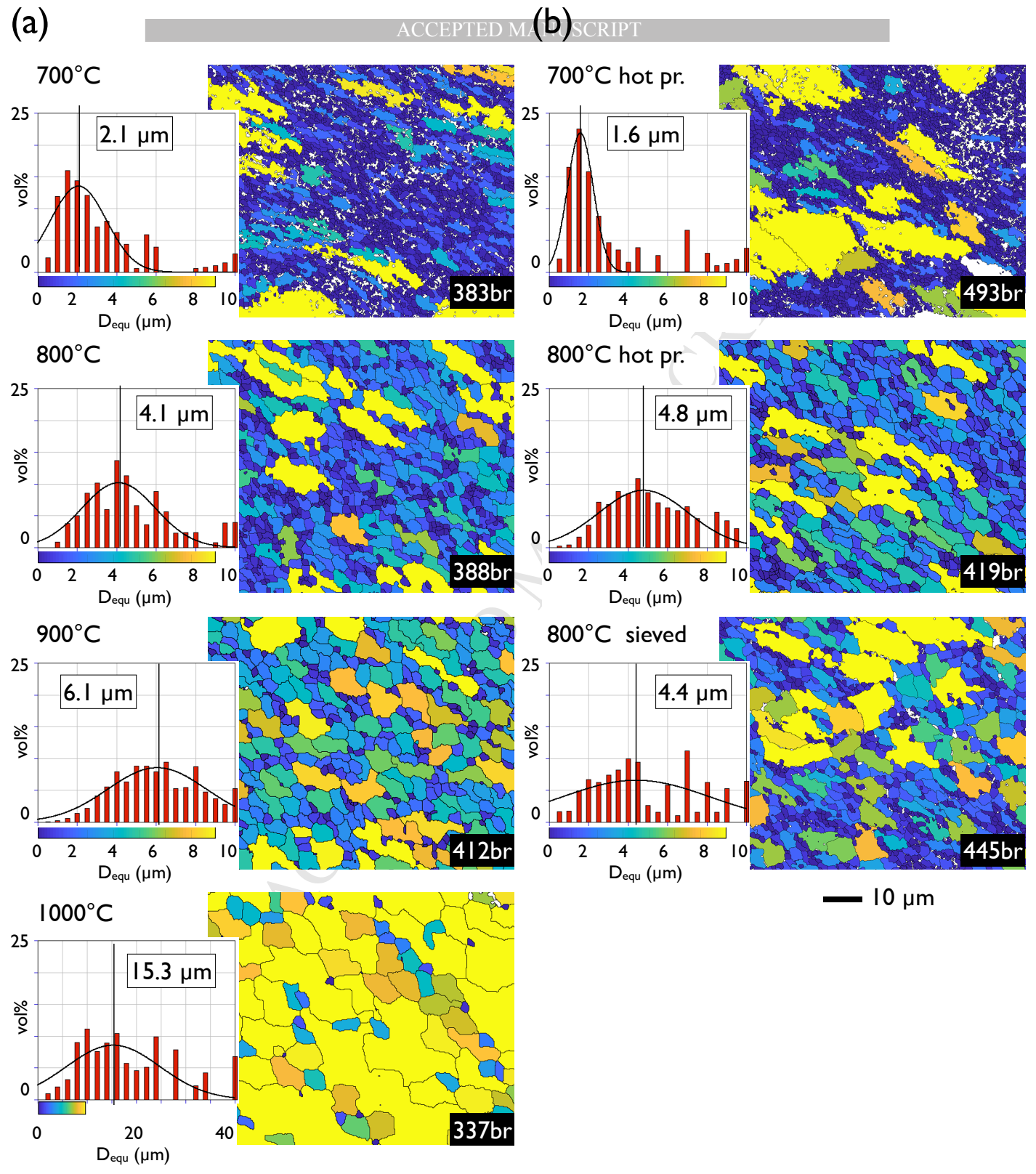

Highlights:

(1) New large data set defines brittle to viscous transition in quartz

(2) Low stress exponent of n = 1.9 + 0.6 between 800C and 1000C for viscous deformation

(3) Viscous deformation by combination of dislocation and diffusion (solution precipitation) creep

(4) Simultaneous diffusion and dislocation creep partition into different grain sizes, shown by CPO

(5) Goetze criterion is confirmed as upper stress limit of viscous deformation